nature COMMUNICATIONS

ARTICLE

Received 19 Sep 2016 | Accepted 30 Jan 2017 | Published 21 Mar 2017

DOI: 10.1038/ncomms14767

OPEN

Periodic potentials in hybrid van der Waals heterostructures formed by supramolecular lattices on graphene

Marco Gobbi[1], Sara Bonacchi[1], Jian X. Lian[2], Yi Liu[3], Xiao-Ye Wang[3], Marc-Antoine Stoeckel[1], Marco A. Squillaci[1], Gabriele D'Avino[2,†], Akimitsu Narita[3], Klaus Müllen[3], Xinliang Feng[4], Yoann Olivier[2], David Beljonne[2], Paolo Samorì[1] & Emanuele Orgiu[1,†]

The rise of 2D materials made it possible to form heterostructures held together by weak interplanar van der Waals interactions. Within such van der Waals heterostructures, the occurrence of 2D periodic potentials significantly modifies the electronic structure of single sheets within the stack, therefore modulating the material properties. However, these periodic potentials are determined by the mechanical alignment of adjacent 2D materials, which is cumbersome and time-consuming. Here we show that programmable 1D periodic potentials extending over areas exceeding $10^4\,\mathrm{nm}^2$ and stable at ambient conditions arise when graphene is covered by a self-assembled supramolecular lattice. The amplitude and sign of the potential can be modified without altering its periodicity by employing photoreactive molecules or their reaction products. In this regard, the supramolecular lattice/graphene bilayer represents the hybrid analogue of fully inorganic van der Waals heterostructures, highlighting the rich prospects that molecular design offers to create *ad hoc* materials.

---

[1] University of Strasbourg, CNRS, ISIS UMR 7006, 8 Allée Gaspard Monge, F-67000 Strasbourg, France. [2] Laboratory for Chemistry of Novel Materials, Center for Research in Molecular Electronics and Photonics, University of Mons, Place du Parc 20, 7000 Mons, Belgium. [3] Max Planck Institute for Polymer Research, Ackermannweg 10, 55128 Mainz, Germany. [4] Center for Advancing Electronics Dresden (CFAED) and Department of Chemistry and Food Chemistry, Technische Universität Dresden, Mommsenstraße 4, 01062 Dresden, Germany. † Present addresses: CNRS, Institut Néel, 25 Rue des Martyrs, F-38042 Grenoble, France (G.D.); Institut National de la Recherche Scientifique (INRS), EMT Center, 1650 Boulevard Lionel-Boulet, J3X 1S2 Varennes, Québec, Canada (E.O.). Correspondence and requests for materials should be addressed to P.S. (email: samori@unistra.fr) or to E.O. (email: emanuele.orgiu@emt.inrs.ca).

Van der Waals (vdW) heterostructures, in which different two-dimensional (2D) materials are superimposed in a stacked configuration, represent a versatile experimental platform to study fundamental properties for device physics and materials science[1–3]. Based on these mechanically assembled stacks, atomically thin novel devices have been demonstrated, such as (tunnelling) transistors[4], p-n and tunnelling diodes[5,6], photovoltaic elements[7] and light emitting diodes (LED)[8].

From a more fundamental point of view, the mutual interaction between vertically-stacked 2D materials generates electronic properties that are different from those of the isolated materials, as experimentally demonstrated for graphene on boron nitride[9–13]. In the latter case, a Moiré pattern develops due to the lattice mismatch between the two materials[14], resulting in a periodic potential (superlattice) with hexagonal geometry capable of modifying profoundly the band structure of graphene. Similarly, other geometries of periodic potentials are predicted to affect the electronic properties of graphene in different ways. For example, a one-dimensional (1D) Kronig–Penney periodic potential with nanoscale periodicity is predicted to create an anisotropic propagation of charge carriers along the different directions of the potential[15]. Hitherto, 1D graphene superlattices that could be pre-programmed with atomic precision have not been demonstrated.

In this context, the use of molecules offers two attractive features. First, organic molecules can prompt doping effects in 2D materials[16–19], causing local modifications of their surface potential[20–22]. Second, these molecules form ordered 2D crystalline structures when physisorbed on graphene and other 2D materials[23–35]. Given the immense opportunities offered by hybrid organic–inorganic vdW heterostructures in modifying the fundamental electronic properties of the pristine materials, the field is still widely unexplored[3]. There are only a few reports connecting doping effects with the specific position of functional groups[26,36–39], and combining molecules and 2D materials for the technological need of forming p–n junctions[40,41].

In this work, we demonstrate that a tunable periodic potential with 1D geometry on graphene can be realized at ambient conditions in a hybrid vdW heterostructure composed of a 2D supramolecular lattice (SL) self-assembled on graphene, with single domains extending over areas exceeding $250 \times 250\,\mathrm{nm}^2$. The amplitude of the periodic potential is mediated by the specific interaction between graphene and molecular dipoles, while the nanoscale periodicity is determined by the geometry of the self-assembly. In particular, by using a photoreactive organic molecule, we show how a subtle photo-induced change in the chemical structure of the starting molecule leads to a different amplitude of the potential, while leaving the periodicity unaltered.

Results

Molecular approach to the formation of periodic potentials. The analogy between hybrid and fully inorganic vdW heterostructures goes beyond their layered nature; in analogy to stacks of inorganic 2D materials, vdW forces drive the interaction between graphene and the self-assembled molecular layer, and similar inter-layer interactions can be envisaged. However, the paradigm leading to the formation of such heterostructure is substantially different. While in inorganic vdW heterostructures the different monolayers are mechanically superimposed with an empirical (optical) alignment[42], in the molecular case a careful choice of the molecular unit allows the spontaneous creation of self-assembled and ordered layers with predictable geometry and atomic precision. Hence, single molecules can be regarded as molecular building blocks (MBBs) that determine both geometry and functionality of the SL.

Our approach is schematically illustrated in Fig. 1a. We design an MBB composed of a head, bearing a light-reactive moiety, and a tail, consisting of a long aliphatic chain. This linear tail drives the molecular self-assembly[43,44] and acts as a spacer between adjacent functional heads, forming a lamellar assembly which determines the 1D periodicity of the potential (see Fig. 1a). Electric fields generated by molecular dipoles within the functional heads are responsible for the modulation of the surface potential of graphene, introducing an electric-field effect analogous to that of a constant external gate, and ultimately determining the amplitude and sign of the periodic potentials. Moreover, the functional headgroup of the photoreactive MBB can be modified before deposition on graphene by simple irradiation in different solvents, yielding new MBBs. Specifically, we used 3-trifluoromethyl-3-(3-octadecyloxyphenyl)diazirine (MBB-1), shown in Fig. 1b, as photoreactive MBB. The diazirine headgroup consists of a carbon bound to two nitrogen atoms, and was selected because it can undergo photolysis very efficiently, forming a reactive carbene and nitrogen gas under irradiation with ultraviolet light (Fig. 1b)[45]. If irradiated in chloroform, the *in situ* generated carbene binds to the solvent molecules in its proximity, generating modified MBBs in a mixture which we call MBB-2. As detailed in the Supplementary Figs 1–3, we found that the main reaction product in the mixture has the structure shown in Fig. 1b, in which a Cl atom substitutes the diazirine moiety. This evidence is further corroborated by a joint optical and electrical characterization (see Supplementary Fig. 4) performed on *ad hoc* synthesized molecules (called P-1 and P-2). Absorption spectra allow to follow the change in the molecular head of MBB-1, as shown in Fig. 1c. After 30 min of irradiation at $\lambda = 365\,\mathrm{nm}$ (areal power density $1.7\,\mathrm{mW\,cm^{-2}}$), the characteristic absorption at $\lambda = 365\,\mathrm{nm}$ of MBB-1 disappears, revealing that MBB-1 was efficiently photolyzed.

Nanoscale characterization of the supramolecular lattices. The periodicity and geometry of the SL-induced potential are determined by the nanoscale molecular arrangement which is investigated through scanning tunneling microscope (STM) imaging. We performed STM imaging in ambient conditions on dry SLs, formed by simply spin-coating a solution of either MBB-1 or MBB-2 (as displayed in Fig. 2a–c or 2d–f, respectively). In view of its atomic flatness over hundreds-of-micrometer-sized terraces, the SL can be mapped with increased spatial resolution on highly ordered pyrolitic graphite (HOPG) substrates (Fig. 2a,b,d,e), yet its motif is identical to that obtained when using graphene grown by chemical vapour deposition (CVD) supported on SiO_2 as substrate (Fig. 2c,f).

The self-assembly is driven by the interplay of molecule–substrate and molecule–molecule interactions; in particular vdW interactions occur between the different alkyl chains, which adsorb flat on graphite/graphene, generating well-defined, crystalline lamellar architectures.

In the case of MBB-1, the functional heads lie close to each other, with the alkyl chains forming an interdigitated structure, exhibiting a unit cell where $a = (3.8 \pm 0.1)\,\mathrm{nm}$, $b = (0.9 \pm 0.1)\,\mathrm{nm}$ and $\alpha = (84 \pm 2)^\circ$ therefore leading to an area $A = (3.4 \pm 0.1)\,\mathrm{nm}^2$, with each unit cell containing two molecules (Fig. 2a). Similar SL structures are also observed for MBB-2 (Fig. 2d). Again, the alkyl chains lie flat on the surface by aligning in interdigitated crystalline structures with a similar unit cell where $a = (3.8 \pm 0.2)\,\mathrm{nm}$, $b = (0.9 \pm 0.1)\,\mathrm{nm}$, $\alpha = (84 \pm 2)^\circ$ giving rise to an area $A = (3.5 \pm 0.2)\,\mathrm{nm}^2$. The nearly identical unit cells are justified if one considers that on ultraviolet irradiation only a few atoms in the molecular head are replaced. Instead, the long alkyl chains are

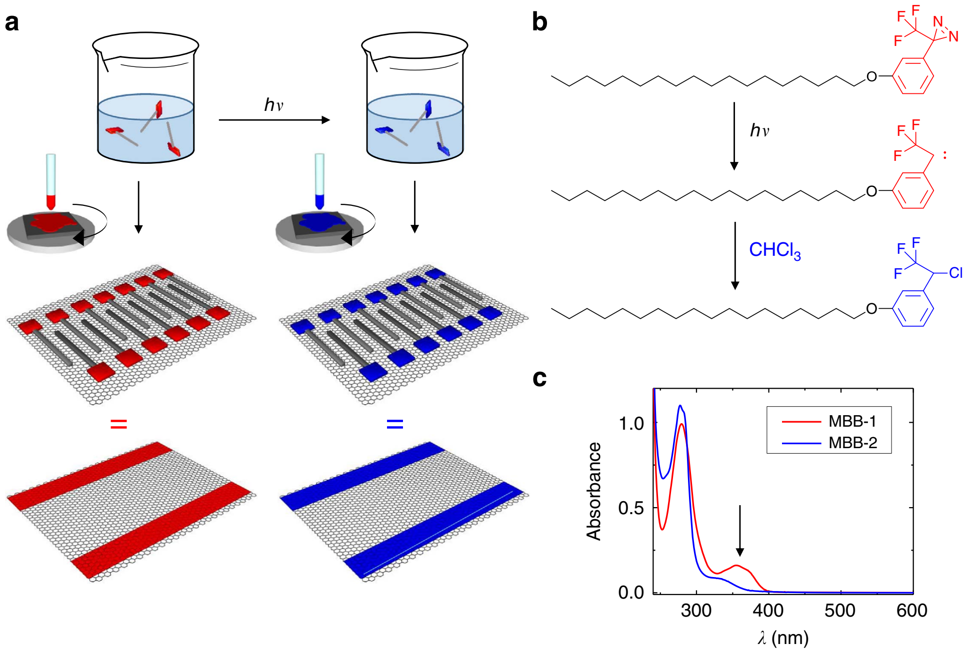

Figure 1 | Cartoon of our approach. (**a**) MBB-1 is formed by a linear alkyl tail (sketched as a grey rod) and a photoreactive diazirine head group (red square). The latter undergoes photolysis under exposure to ultraviolet light in chloroform ($CHCl_3$) solution forming different reaction products in a mixture (MBB-2) with modified head groups (blue squares). Molecular self-assembly occurs by spin-coating a solution of MBB-1 or MBB-2 on graphene's surface giving rise to supramolecular lattices with identical unit cell for MBB-1 and MBB-2. However, the head groups in MBB-1 and MBB-2 induce different gating effects, resulting in 1D periodic potentials with different amplitude (blue versus red) but with the same 1D periodicity. (**b**) Chemical structures of the molecules. The main reaction product obtained by ultraviolet irradiation in $CHCl_3$ is shown in blue, while other products are listed in Supplementary Figs 1–3. (**c**) *In situ* monitoring of the photolysis through ultraviolet–visible spectroscopy (concentration of MBB-1: 2.2×10^{-3} M in $CHCl_3$; path length: 2 mm (quartz cell); room temperature). In particular, absorption spectra of MBB-1 (red) and MBB-2 (blue) are shown before and after ultraviolet irradiation at $\lambda = 365$ nm for 30 min.

unaltered in both cases. Hence, MBB-1 and MBB-2 form SLs that possess the same lattice parameters but differ in the head groups, resulting in different electronic interactions with graphene.

For both MBB-1 and MBB-2, crystalline domains with different orientations of the lamellae may form on the graphene surface. This evidence reflects the three-fold symmetry of the substrate and may give rise to misorientation in the direction of the 1D potential. Therefore the size of single-crystalline domains is a key parameter for the relevance of this study on the device physics. To gain detailed insight into this issue, we recorded survey STM images mapping the surface over a scale of a few hundred nanometres. Figure 2b,e show large-area STM images of MBB-1 and MBB-2, respectively. In both cases, an ordered array of lamellae with only one orientation extends over the whole image. Domains with different orientations could be observed in other large-area STM images. After careful analysis of 15 large-area STM images for each MBB, we can conclude that the typical single-domain size is ~300 nm × 300 nm, as shown in Supplementary Fig. 5 and in Supplementary Table 1. Compared with the length scale relevant for the charge transport in graphene, these single domains are typically two orders of magnitude larger than the typical size of the potential puddles that are responsible for limiting the mobility at the graphene/SiO_2 interfaces[46]. Moreover, such area is still suitable for nano-fabrication and optical/spectral inspection of the physical properties generated by the presence of the SLs. The assembly of MBB-1 and MBB-2 was investigated also on CVD graphene on SiO_2 to consider a situation closer to that of the actual devices, as shown in the Fig. 2c,f. In this case, the image resolution is lower, due to the intrinsic roughness of the underlying SiO_2 substrate. However, even on CVD graphene, it is possible to clearly observe the existence of ordered lamellar structures whose size is in good agreement with that monitored on HOPG. This finding confirms that the MBBs assemble in the same way on both HOPG and graphene/SiO_2. Large-size STM images show that the crystalline order is maintained over wide areas even on CVD graphene on SiO_2, as displayed in the Supplementary Fig. 5 for MBB-2. We stress that the STM images in Fig. 2 were measured in air at room temperature and that crystalline domain size and orientation were found to be unchanged even after several hours of continuous acquisition. Moreover, STM images revealed that the unit cell of the molecular assemblies recorded within a few minutes after the SL formation would be identical (within experimental error) to those recorded a few days later. Indeed, the formation of a tight molecular packing along with the strong interaction with graphene promoted by the long alkyl chains would hinder molecular diffusion and thus stabilize the assembly.

Electrical characterization of devices. To determine whether the molecules are effectively introducing a potential, we study the doping caused by the different SLs on graphene-based field-effect devices (see the 'Methods' section for details on the device fabrication). The devices were measured before and after the formation of the MBB-1 and MBB-2 SLs, to evaluate their effect on the electrical characteristics of graphene. The measurements were reproduced on three different devices for each MBB, and the results were in qualitative and quantitative agreement (see the 'Methods' section for details). Representative dependence of the drain current I_{DS} on the gate voltage V_{GS} is displayed in Fig. 3. In the case of MBB-1 (Fig. 3a), the charge neutrality point was not shifted significantly by the presence of the SL, indicating minor doping effects. Interestingly, the hole mobility increased after the formation of the SL (from 2,200 to 2,650 $cm^2 V^{-1} s^{-1}$ for the device in Fig. 3a). The increase in mobility was directly related to the presence of the SL, since the initial electrical characteristics of the clean graphene were recovered after the molecules were washed away by rinsing the sample with $CHCl_3$, and the mobility decreased to its initial value (see the Fig. 3a).

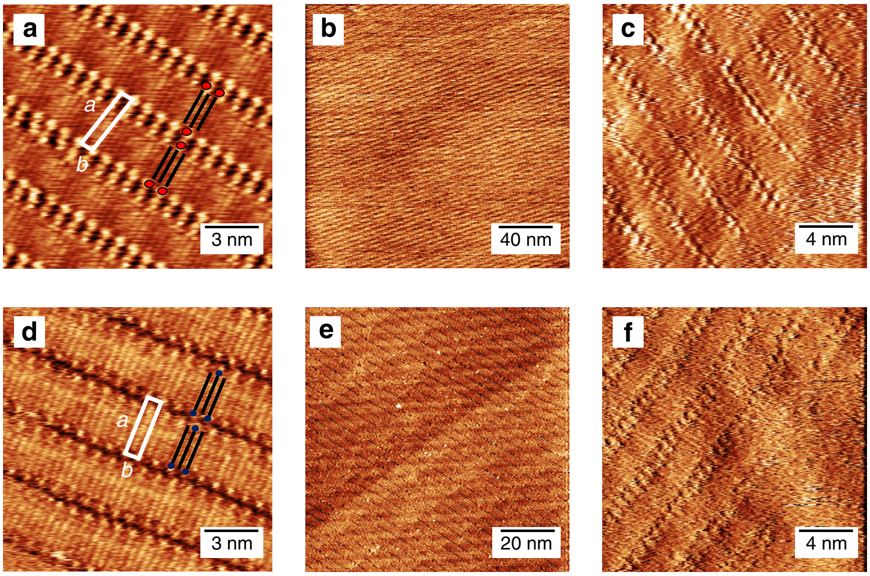

Figure 2 | Scanning tunnelling microscopy images of supramolecular lattices. (**a**–**c**) MBB-1 (**d**–**f**) MBB-2. (**a**,**b**,**d**,**e**) Images recorded on highly oriented pyrolytic graphite, the height channel is shown; (**c**,**f**) Images recorded on graphene over SiO_2, current channel is shown. The images were recorded by using the following tunnelling parameters: (**a**,**b**) tip voltage $V_t = 400$ mV and average tunnelling current $I_t = 20$ pA; (**c**) $V_t = -600$ mV, $I_t = 40$ pA; (**d**,**e**) $V_t = 400$ mV, $I_t = 40$ pA; and (**f**) $V_t = 400$ mV, $I_t = 10$ pA.

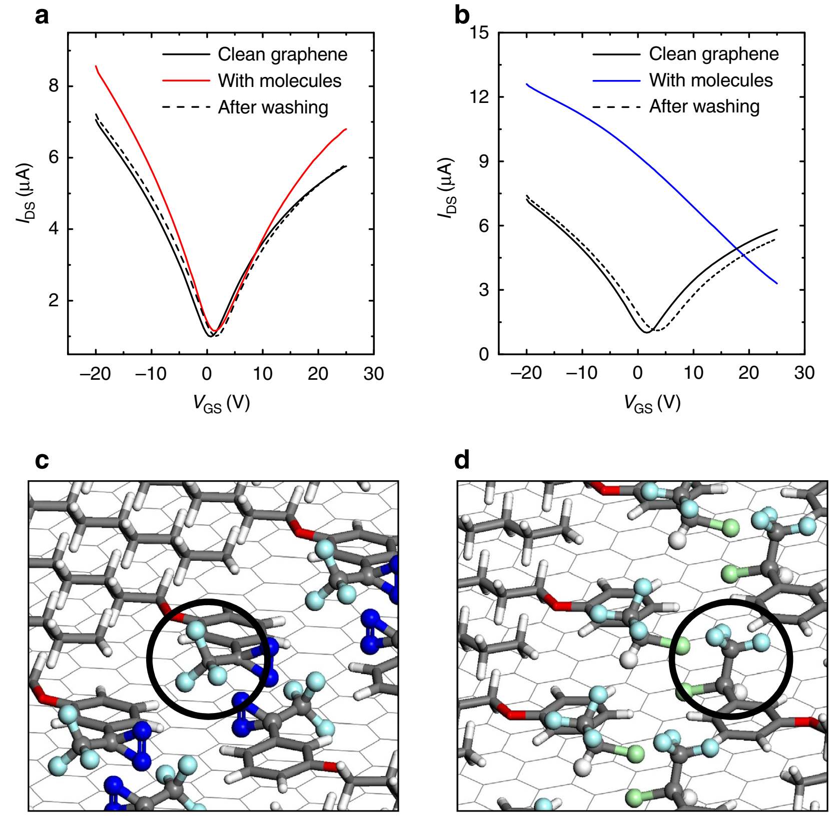

Figure 3 | Effect of supramolecular lattices onto the electrical characteristics of graphene. (**a**,**b**) Electrical characteristics of a clean device and of the same device after the formation of MBB-1 (**a**) and MBB-2 (**b**) supramolecular lattices. I_{DS} is the drain current, and V_{GS} is the gate potential. (**c**,**d**) Zoom of the optimized supramolecular lattice at the functional head groups for (**c**) MBB-1 and (**d**) MBB-2. In **c**,**d**, the position of the CF_3 groups is highlighted by a black circle. Carbon atoms are shown in grey, hydrogen in white, oxygen in red, nitrogen in dark blue, fluorine in light blue and chlorine in green. As a scale reference, the distance between adjacent carbon atoms in the graphene substrate is 1.4 Å.

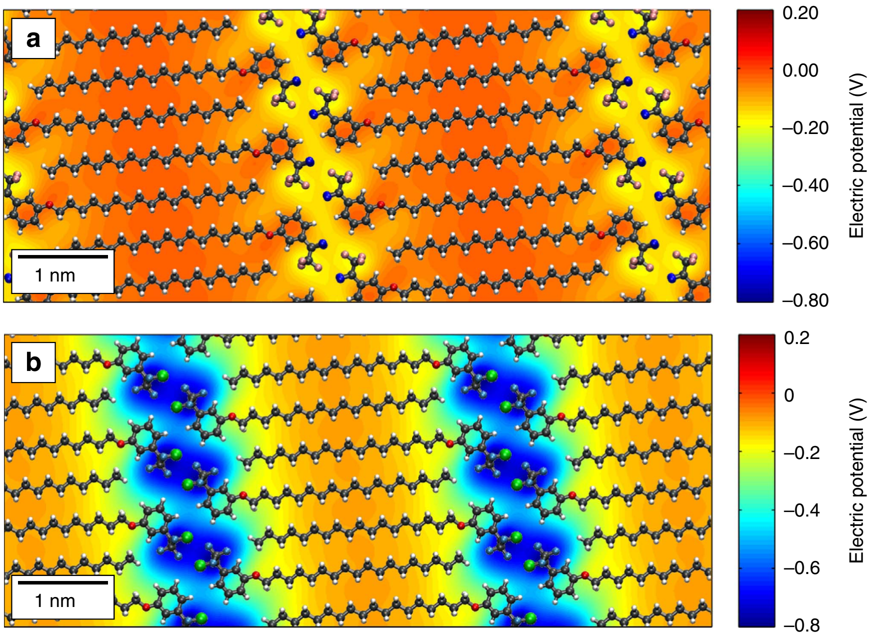

Figure 4 | Periodic potentials introduced by the supramolecular lattices. Calculated differential electrical potential induced by a supramolecular lattice of (**a**) MBB-1 and (**b**) MBB-2 on graphene. The supramolecular lattice is superimposed for clarity. The electrical potential is periodically modulated, with negative values in the region below the molecular heads. Carbon atoms are shown in grey, hydrogen in white, nitrogen in red, fluorine in light blue and chlorine in green.

In the case of MBB-2, after the formation of the SL the charge neutrality point was shifted towards positive voltages ($\Delta V > 25\,\mathrm{V}$), as shown in Fig. 3b. This effect corresponds to hole accumulation in the graphene channel, with an induced charge density of $\Delta p > 5 \times 10^{12}\,\mathrm{cm}^{-2}$, according to the widely used parallel-plane capacitor model[36]. The electrical characterization provides unambiguous evidence that the effect of the MBB-2 SL–averaged over several randomly oriented domains–is analogous to that of a (fixed) top gate. Moreover, the electrical characterization demonstrates that the doping effect is solely determined by the head group, which is the only part of the MBB modified by the ultraviolet irradiation.

Generally, our devices possess a channel length of a few micrometres that is wider than the typical size of a single domain. As a consequence, our measurements probe not a single but rather a few domains with different random orientations, which impedes measuring the anisotropy in electrical conductance possibly induced by the SL. However, the information extracted by the electrical characterization provides very useful insight on effects, averaged over several randomly oriented domains, associated with the formation of the hybrid vdW heterostructure. While the STM nanoscale characterization provides information about the geometry and periodicity of the potential, the information extracted through device characterization is related to the amplitude of the periodic potential. The demonstration of anisotropy in the conductance of graphene would require a miniaturization of devices that is beyond the scope of this work. To better quantify the effects on the nanoscale electrical properties in presence of the SL, we have performed conductive atomic force microscopy (C-AFM) measurements on a contacted graphene flake, acting as the device active layer, before and after formation of a MBB-1-SL. After formation of the SL, some inhomogeneities in the conductance are introduced with a length scale of a few hundred nanometres, which is the typical size of the single domains imaged by STM. Although the lamellas cannot be visualized by C-AFM, this finding supports the presence of anisotropic conductance within graphene covered by a single-domain SL, as detailed in Supplementary Fig. 6.

Nanoscale origin of the doping effect. To gain more insight into the origin of the doping effects, the interactions of the molecular assembly with graphene were elucidated through molecular mechanics/molecular dynamics (MM/MD) simulations. For the case of MBB-2, we assumed that all the molecules at the surface possess the structure shown in Fig. 1b, following the findings described in Supplementary Figs 1–4. For both the assembly of MBB-1 and MBB-2, (MM/MD) simulations show that the alkyl chains are interdigitated and the carbon backbones are lying parallel to the graphene surface. The lattice parameters of the calculated unit cell in both cases, that is MBB-1 and MBB-2, are the same, in agreement with the experimental data (see Supplementary Fig. 7). From a closer look at the functional head groups of the calculated assemblies, a major difference appears between the positioning of the molecular head in MBB-1 versus MBB-2 (see Fig. 3c,d). In the former, the diazirine moiety is lying flat on graphene, so that the CF_3 group is pointing parallel to graphene, whereas the axis of the $N=N$ double bond is normal to the graphene plane (Fig. 3c). Conversely, the CF_3 unit of MBB-2 is pointing in the z-direction normal to the graphene surface (Fig. 3d). Interestingly, such a difference in the orientation of the functional head groups has very limited impact on the overall organization of the molecular adlayer assembly, but it drastically affects the intrinsic dipole moment of the SLs in the z-direction. Indeed, in the MBB-1 case the molecules are almost parallel to the graphene surface, so that a small net dipole moment per molecule is expected perpendicular to the surface (Fig. 3c). Instead, in the MBB-2 case, a larger vertical dipole arises from the CF_3 groups, which are found to be almost perpendicular to the graphene layer (Fig. 3d). Based on this observation, one can qualitatively understand the p-type doping measured in graphene with the MBB-2 adlayer. The electric-field generated by the vertical dipoles acts as a top gate and increases the work function of graphene, effectively inducing p-type doping. At a more quantitative level, density functional theory (DFT) calculations made it possible to estimate the doping induced by the two SLs on the basis of their calculated arrangement, as detailed in Supplementary Methods and Supplementary Figs 8–11.

More specifically, molecular doping of graphene is usually sourced by two effects[17,47], namely charge transfer from the molecules, and the presence of molecular dipoles exerting a local gating. DFT calculations allow to disentangle these two contributions for each SL and demonstrate that the charge transfer contribution is almost identical in both cases. Instead, in the case of MBB-1 the calculated vertical molecular dipole is rather low ($\mu_z = -0.17\,\mathrm{D\,mol^{-1}}$), while in the case of MBB-2 it is significantly higher ($\mu_z = -0.82\,\mathrm{D\,mol^{-1}}$). The doping effect in the MBB-2 case, therefore, results from the higher vertical dipole moment of the SLs, as expected from the geometry of the assembly. By accounting for molecular motion at room temperature from MD simulations, we predict a negligible and a significant work function shift for MBB-1 and MBB-2, respectively, as experimentally verified by photoemission spectroscopy in air (see Supplementary Fig. 12). The work function shift is accompanied by an induced p-type doping for MBB-2 (on the order of $\Delta p = 5 \times 10^{12}\,\mathrm{cm^{-2}}$) and a minor p-type doping for MBB-1 ($\Delta p < 5 \times 10^{11}\,\mathrm{cm^{-2}}$), in excellent agreement with the device experiments. Moreover, our theoretical analysis confirms that the origin of the measured effects can be entirely ascribed to the geometry of the head groups, while the assembly of the alkyl chains, similar for MBB-1 and MBB-2, is not a source of doping.

Spatially resolved electrostatic potential. Proceeding with the analysis, the spatially resolved electrostatic potential at the graphene/molecule interface was calculated by means of classical microelectrostatic calculations (see Supplementary Methods for details).

In Fig. 4a,b we show the differential potential V ($z = 8$ Å)–V ($z = 0$ Å) for both MBB-1 and MBB-2, where V ($z = 8$ Å) is the potential calculated on the parallel plane just above the SLs, and V ($z = 0$ Å) is the potential at the graphene surface. Such differential potential probes the dipolar field associated with the out-of-plane component of the molecular dipoles and has an effect similar to that of a fixed externally applied gate voltage. In both assemblies, such induced gating potential is characterized by a 1D-modulation, with higher negative values localized at the molecular heads separated by inert alkyl chains. The amplitude of the induced gating effect increases by a factor of 4 from MBB-1 to MBB-2, as expected on the basis of the different vertical dipoles. Note that image charge and depolarization effects associated with intermolecular interactions have been estimated using DFT electronic structure calculations implementing periodic boundary conditions. These were found to reduce the electric dipole per molecule by ~30% for MMB-1 and 20% for MBB-2. Thus, image effects are found to be fairly limited in our case and the graphene layer acts primarily as a template breaking up symmetry in picking selected dipolar conformations for the MBBs at the surface, which then translates into the observed electrostatic potential shown in Fig. 4.

This different amplitude induced by the MBB-1 and MBB-2 SL demonstrates the ability of introducing significant variations in the SL-induced periodic grating with a subtle light-induced change in the molecular structure. In both cases, the in-plane distribution of the potential can be considered as a nanoscopic experimental realization of a Kronig–Penney potential. We highlight that not only its geometry, but also its amplitude is within the same order of magnitude of that considered in the initial prediction of anisotropic behaviour of charge carriers in graphene superlattices[15].

Modification of the periodic potential. Finally, we show that periodic potentials with the same geometry but different intensity can be achieved by preparing SLs of MBB-1 after ultraviolet irradiation in different solvents. To prove further this concept, we present here a detailed nanoscale and electrical characterization of MBB-1 after ultraviolet irradiation in diethylamine, which results in a mixture hereafter referred to as MBB-3. The assembly of MBB-3 is shown in Fig. 5a,b on HOPG and CVD graphene, respectively. Similarly to MBB-1 and MBB-2, MBB-3 self-assembles forming ordered lamellae in which the functional heads lie close to each other, with the alkyl chains forming an interdigitated structure. The unit cell parameters were $a = (3.8 \pm 0.2)\,\mathrm{nm}$, $b = (0.9 \pm 0.1)\,\mathrm{nm}$ and $\alpha = (84 \pm 2)°$ which lead to an area $A = (3.5 \pm 0.2)\,\mathrm{nm^2}$, analogous to that of MBB-1 and MBB-2. Again, the atoms incorporated through photolysis do not perturb the assembly at the nanoscale, which is determined and imposed by the alkyl chains. Instead, the intensity of the induced potential is determined by the interaction with the head groups. The overall effect can be measured in a three-terminal device, by covering a graphene device with a MBB-3 SL. In this case (Fig. 5c), the charge neutrality point shifts towards negative values, corresponding to electron accumulation (n-doping) in the graphene channel. A shift in the charge neutrality point $\Delta V = -11\,\mathrm{V}$ corresponds to an induced electron density $\Delta n = 2.6 \times 10^{12}\,\mathrm{cm^{-2}}$. Even in this case, the electrical properties of the clean graphene are recovered when the molecules are washed away from the graphene surface with a simple rinsing step in chloroform.

Interestingly, the effect on the $I_{DS} - V_{GS}$ traces of graphene is opposite to that of MBB-2. Since the induced periodic potential is primarily determined by the orientation of local molecular

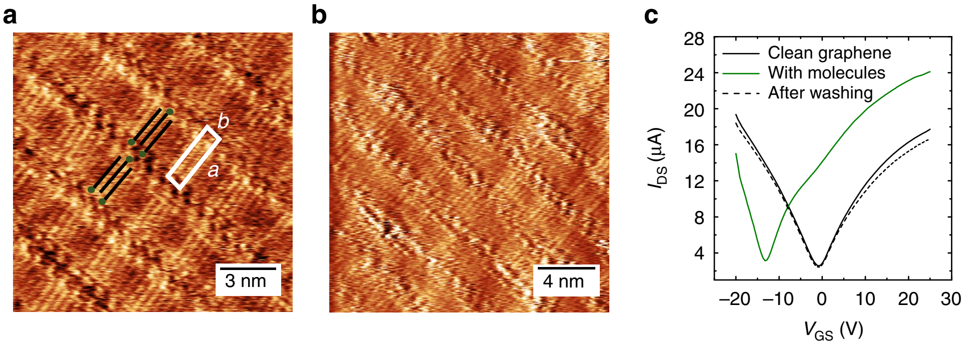

Figure 5 | Modification of the periodic potential. Scanning tunnelling microscopy images of the nanoscale assembly of MBB-3 on different substrates: (**a**) on highly oriented pyrolytic graphite (height channel) and (**b**) on graphene over SiO_2 (current channel). The images were recorded by using the following tunnelling parameters: (**a**) $V_t = -400\,\mathrm{mV}$, $I_t = 20\,\mathrm{pA}$; (**b**) $V_t = 600$, $I_t = 60\,\mathrm{pA}$. The effect of the SL formed by MBB-3 on the electrical characteristics of a graphene device is shown in **c**. I_{DS} is the drain current, and V_{GS} is the gate potential.

dipoles, one is thus led to conclude that the sign of such a potential for MBB-3 is opposite to that of MBB-2.

Discussion

The concept that interplanar interactions are capable of modifying fundamental electronic properties of pristine materials lies at the heart of the research field of vdW heterostructures. In this context, the possibility of introducing tunable 1D potentials through organic SLs is particularly appealing. For instance, one could combine graphene covered by a SL with other inorganic 2D materials to fabricate more complex multi-layered hybrid vdW heterostructures. In such systems, an ordered lamellar assembly modifying the momentum dispersion of graphene would induce anisotropy not only on the in-plane (graphene) but also on the inter-layer charge transport, for which momentum conservation plays an important role[48]. Moreover, a fully anisotropic heterostructure might be obtained by combining our SL-covered graphene with other 2D materials intrinsically possessing 1D anisotropy (such as ReS_2 (ref. 49) and black phosphorus[50]) to demonstrate novel device architectures actively exploiting charge transport along a preferential direction. Finally, we point out that bottom–up supramolecular approaches for the realization of periodic potentials is not limited to graphene, since analogous molecules form ordered 1D assemblies also on the surface of other 2D materials[51], widening the horizons of the present study. For instance, a SL similar to those described in this study assembled on semiconducting transition metal dichalcogenides (such as WSe_2 and MoS_2) might introduce a 1D periodic potential capable of locally varying the position of the Fermi level, resulting in alternating hole- or electron- rich regions. In this way, one would obtain a series of consecutive nanoscale p–n junctions with distinctive charge transport properties and optical response.

In conclusion, our study shows that organic SLs represent an ideal system for generating periodic potentials whose periodicity, amplitude and sign can be pre-programmed by careful molecular design. In particular, here we have shown that a periodic potential with 1D geometry can be generated at the graphene surface and manipulated by making use of molecular photo-reactivity. In perspective, a 1D potential will offer the opportunity to introduce anisotropy in otherwise isotropic materials, hence paving the way for design and implementation of novel functional vdW heterostructures, for example, for 1D charge transport. The control over periodic potentials can hardly be achieved in vdW heterostructures based solely on inorganic 2D materials, while their combination with SLs allows expanding substantially the 2D material library. Chemistry can offer an almost unlimited choice of SL that can form hybrid vdW heterostructures with controllable structural and electronic properties, exerting periodic potentials with tunable amplitude and periodicity. In perspective, a great deal of novel electrical, magnetic, piezoelectric and optical functionalities arising from such hybrid vdW heterostructures are expected by taking full advantage of the infinite degrees of freedom offered by the design of the MBBs.

Methods

Sample preparation. Full details regarding the characterization and synthesis of the MBBs are given in Supplementary Figs 13–19 and in Supplementary Note 1.

Ultraviolet–visible spectroscopy. Absorption spectra were recorded at room temperature ($\sim 25\,^{\circ}C$) with a JASCO V-670 spectrophotometer and all solutions were examined in quartz cells with 2-mm pathlength (HELLMA) with a concentration of 2.2×10^{-3} M. Photochemical reaction of MBB-1 was performed in air-equilibrated $CHCl_3$ (Uvasol Merck-Millipore) or in degassed diethyalmine (Sigma-Aldrich) by using an Ultraviolet lamp (UV-6 L/M Herolab) with $\lambda_{irr} = 365$ (± 5) nm and a power density $= 1.7\,mW\,cm^{-2}$.

Device fabrication and characterization. Back gated devices were fabricated on Si/SiO_2 (90 nm) substrates with a Microtech laser writer, exposing with a $\lambda = 405$ nm laser a standard photoresist (AZ1505, Microchemicals). Gold (without adhesion layer) was thermally evaporated onto the patterned photoresist and lift-off was carried out in warm acetone (40 °C). After fabrication, the devices were immersed in warm NMP (40 °C) overnight, rinsed with chloroform, acetone and isopropanol. The devices were kept in a nitrogen-filled glove box in which they could be measured in a probe station connected to a Keithley 2636. By employing this procedure, the graphene device showed almost-ideal, symmetric and stable current–voltage $I_{DS} - V_{GS}$ characteristics, with the charge neutrality point close to a gate voltage $V_{GS} = 0$ V, and hole mobility reproducibly above $1{,}800\,cm^2\,V^{-1}\,s^{-1}$. The carrier mobility was determined by the conventional parallel-plane capacitor model:

$$\mu = \left| \frac{dI_{DS}}{dV_{GS}} \right| \frac{L}{W} \frac{t}{\varepsilon_0 \varepsilon_r}$$

where L and W are the graphene channel length and width, t is the thickness of gate oxide, ε_r is the relative dielectric permittivity of SiO_2. The mobility was extracted at the carrier concentration value of $|n| = 1 \times 10^{12}\,cm^{-2}$, by measuring dI_{DS}/dV_{GS} at 4.5 V away from the charge neutrality point. In all the electrical measurements, the potential applied between the graphene electrodes was $V = 10$ mV. The reproducibility of the effect of each SL on the electrical characteristics of devices was tested by repeating the measurement on three different devices for each MBB. For every test, a fresh solution of MBB was employed. The doping effect is reproducible: MBB-1 was found to induce small p-type doping ($\Delta V < 5$ V in the three tested devices); MBB-2 significantly higher p-type doping ($\Delta V > 25$ V in the three tested devices); and MBB-3 n-type doping (ΔV in the range between -7 and -12 V in the three tested devices). Moreover, the experiments were repeated several times on the same device, by washing the MBBs away and re-forming the SL. In the cases of MBB-1 and MBB-3, the increase in mobility after the formation of the SL was also found in the three tested devices.

Supramolecular lattice formation. To form the SLs, molecules were spin-coated onto either HOPG or CVD graphene on SiO_2 and onto devices from chloroform solutions ($1\,mg\,ml^{-1}$). For the sake of consistency, the solutions were spin-coated onto the graphene devices by employing the same parameters used for the STM imaging. In the case of irradiation in diethylamine, the molecules were dried after irradiation and re-solubilized in chloroform before spin-coating. In the case of devices, the solution were spin-coated *in situ* in the nitrogen-filled glovebox. The SLs could be washed away by rinsing the substrates or the devices with $CHCl_3$.

Scanning tunneling microscopy. STM measurements were carried out by using a Veeco scanning tunneling microscope (multimode Nanoscope III, Veeco) operating with an A piezoelectric scanner which allowed the mapping of a maximum area of $1\,\mu m \times 1\,\mu m$. As substrates, we used highly oriented pyrolytic graphite and commercial CVD graphene supported on Si/SiO_2 (300 nm) purchased from Graphenea. The graphene sample has been used as received, without any additional cleaning step, and has been stored in air for 4 months before the STM experiments. The substrates were glued onto a magnetic disk and an electric contact was made with (conductive) silver paint (Aldrich Chemicals).

The STM tips were mechanically cut from a Pt/Ir wire (90/10, diameter 0.25 mm). The images were obtained in air at room temperature. The raw STM data were processed through the application of background flattening, and in the case of the HOPG substrates in Figs 2a,d and 5a the drift of the piezo was corrected using the underlying graphite lattice as a reference. The lattice of the underlying substrate was visualized by lowering the bias voltage V_t to 10 mV and setting the average tunneling current $I_t = 60$ pA. Tip height and current were measured for all STM images.

MD/MM and DFT calculations. Full details regarding the MD/MM and DFT calculations are given in Supplementary Methods and in Supplementary Table 2.

Data availability. The data that support the findings of this study are available from the corresponding authors on request.

References

1. Geim, A. K. & Grigorieva, I. V. Van der Waals heterostructures. *Nature* **499,** 419–425 (2013).
2. Novoselov, K. S., Mishchenko, A., Carvalho, A. & Castro Neto, A. H. 2D materials and van der Waals heterostructures. *Science* **353,** aac9439 (2016).
3. Jariwala, D., Marks, T. J. & Hersam, M. C. Mixed-dimensional van der Waals heterostructures. *Nat. Mater.* **16,** 170–181 (2017).
4. Britnell, L. *et al.* Field-effect tunneling transistor based on vertical graphene heterostructures. *Science* **335,** 947–950 (2012).
5. Lee, C.-H. *et al.* Atomically thin p–n junctions with van der Waals heterointerfaces. *Nat. Nanotechnol.* **9,** 676–681 (2014).
6. Britnell, L. *et al.* Resonant tunnelling and negative differential conductance in graphene transistors. *Nat. Commun.* **4,** 1794 (2013).

7. Britnell, L. *et al.* Strong light-matter interactions in heterostructures of atomically thin films. *Science* **340,** 1311–1314 (2013).
8. Withers, F. *et al.* Light-emitting diodes by band-structure engineering in van der Waals heterostructures. *Nat. Mater.* **14,** 301–306 (2015).
9. Ponomarenko, L. A. *et al.* Cloning of Dirac fermions in graphene superlattices. *Nature* **497,** 594–597 (2013).
10. Dean, C. R. *et al.* Hofstadter's butterfly and the fractal quantum Hall effect in moiré superlattices. *Nature* **497,** 598–602 (2013).
11. Hunt, B. *et al.* Massive Dirac fermions and Hofstadter butterfly in a van der Waals heterostructure. *Science* **340,** 1427–1430 (2013).
12. Gorbachev, R. V. *et al.* Detecting topological currents in graphene superlattices. *Science* **346,** 448–451 (2014).
13. Wang, L. *et al.* Evidence for a fractional fractal quantum Hall effect in graphene superlattices. *Science* **350,** 1231–1234 (2015).
14. Yankowitz, M. *et al.* Emergence of superlattice Dirac points in graphene on hexagonal boron nitride. *Nat. Phys.* **8,** 382–386 (2012).
15. Park, C.-H., Yang, L., Son, Y.-W., Cohen, M. L. & Louie, S. G. Anisotropic behaviours of massless Dirac fermions in graphene under periodic potentials. *Nat. Phys.* **4,** 213–217 (2008).
16. Schedin, F. *et al.* Detection of individual gas molecules adsorbed on graphene. *Nat. Mater.* **6,** 652–655 (2007).
17. Wehling, T. O. *et al.* Molecular doping of graphene. *Nano Lett.* **8,** 173–177 (2008).
18. Liu, H., Liu, Y. & Zhu, D. Chemical doping of graphene. *J. Mater. Chem.* **21,** 3335–3345 (2011).
19. Samuels, A. J. & Carey, J. D. Molecular doping and band-gap opening of bilayer graphene. *ACS Nano* **7,** 2790–2799 (2013).
20. Cervenka, J. *et al.* Graphene field effect transistor as a probe of electronic structure and charge transfer at organic molecule-graphene interfaces. *Nanoscale* **7,** 1471–1478 (2014).
21. Hapala, P. *et al.* Mapping the electrostatic force field of single molecules from high-resolution scanning probe images. *Nat. Commun.* **7,** 11560 (2016).
22. Wickenburg, S. *et al.* Tuning charge and correlation effects for a single molecule on a graphene device. *Nat. Commun.* **7,** 13553 (2016).
23. Prado, M. C. *et al.* Two-dimensional molecular crystals of phosphonic acids on graphene. *ACS Nano* **5,** 394–398 (2011).
24. Wang, Q. H. & Hersam, M. C. Room-temperature molecular-resolution characterization of self-assembled organic monolayers on epitaxial graphene. *Nat. Chem.* **1,** 206–211 (2009).
25. Deshpande, A. *et al.* Self-assembly and photopolymerization of sub-2 nm one-dimensional organic nanostructures on graphene. *J. Am. Chem. Soc.* **134,** 16759–16764 (2012).
26. Zhang, T. *et al.* Self-assembled 1-octadecanethiol monolayers on graphene for mercury detection. *Nano Lett.* **10,** 4738–4741 (2010).
27. Järvinen, P. *et al.* Molecular self-assembly on graphene on SiO$_2$ and h-BN substrates. *Nano Lett.* **13,** 3199–3204 (2013).
28. Riss, A. *et al.* Imaging and tuning molecular levels at the surface of a gated graphene device. *ACS Nano* **8,** 5395–5401 (2014).
29. Tsai, H.-Z. *et al.* Molecular self-assembly in a poorly screened environment: F$_4$TCNQ on graphene/BN. *ACS Nano* **9,** 12168–12173 (2015).
30. Mali, K. S., Greenwood, J., Adisoejoso, J., Phillipson, R. & De Feyter, S. Nanostructuring graphene for controlled and reproducible functionalization. *Nanoscale* **7,** 1566–1585 (2015).
31. Alaboson, J. M. P. *et al.* Templating sub-10 nm atomic layer deposited oxide nanostructures on graphene via one-dimensional organic self-assembled monolayers. *Nano Lett.* **13,** 5763–5770 (2013).
32. Macleod, J. M. & Rosei, F. Molecular self-assembly on graphene. *Small* **10,** 1038–1049 (2014).
33. Zeng, M. *et al.* Self-assembly of graphene single crystals with uniform size and orientation: the first 2D super-ordered structure. *J. Am. Chem. Soc.* **138,** 7812–7815 (2016).
34. Huang, H., Chen, S., Gao, X., Chen, W. & Wee, A. T. S. Structural and electronic properties of PTCDA thin films on epitaxial graphene. *ACS Nano* **3,** 3431–3436 (2009).
35. Zhou, H. T. *et al.* Direct imaging of intrinsic molecular orbitals using two-dimensional, epitaxially-grown, nanostructured graphene for study of single molecule and interactions. *Appl. Phys. Lett.* **99,** 2009–2012 (2011).
36. Li, B. *et al.* Toward tunable doping in graphene FETs by molecular self-assembled monolayers. *Nanoscale* **5,** 9640–9644 (2013).
37. Zhang, X. *et al.* Supramolecular chemistry on graphene field-effect transistors. *Small* **10,** 1735–1740 (2014).
38. Yu, Y. *et al.* Epitaxially self-assembled alkane layers for graphene electronics. *Adv. Mater.* **29,** 1603925 (2017).
39. Phillipson, R. *et al.* Tunable doping of graphene by using physisorbed self-assembled networks. *Nanoscale* **8,** 20017–20026 (2016).
40. Vélez, S. *et al.* Gate-tunable diode and photovoltaic effect in an organic–2D layered material p–n junction. *Nanoscale* **7,** 15442–15449 (2015).
41. Jariwala, D. *et al.* Hybrid, Gate-tunable, van der Waals p – n heterojunctions from pentacene and MoS$_2$. *Nano Lett.* **16,** 497–503 (2016).
42. Castellanos-Gomez, A. *et al.* Deterministic transfer of two-dimensional materials by all-dry viscoelastic stamping. *2D Mater.* **1,** 011002 (2014).
43. De Feyter, S. & De Schryver, F. C. Self-assembly at the liquid/solid interface: STM reveals. *J. Phys. Chem. B* **109,** 4290–4302 (2005).
44. De Feyter, S. & De Schryver, F. C. Two-dimensional supramolecular self-assembly probed by scanning tunneling microscopy. *Chem. Soc. Rev.* **32,** 139–150 (2003).
45. Lawrence, E. J. *et al.* 3-Aryl-3-(trifluoromethyl)diazirines as versatile photoactivated 'linker' molecules for the improved covalent modification of graphitic and carbon nanotube surfaces. *Chem. Mater.* **23,** 3740–3751 (2011).
46. Zhang, Y., Brar, V. W., Girit, C., Zettl, A. & Crommie, M. F. Origin of spatial charge inhomogeneity in graphene. *Nat. Phys.* **5,** 722–726 (2009).
47. Wehling, T. O., Lichtenstein, A. I. & Katsnelson, M. I. First-principles studies of water adsorption on graphene: the role of the substrate. *Appl. Phys. Lett.* **93,** 202110 (2008).
48. Massicotte, M. *et al.* Photo-thermionic effect in vertical graphene heterostructures. *Nat. Commun.* **7,** 12174 (2016).
49. Lin, Y. C. *et al.* Single-layer ReS$_2$: two-dimensional semiconductor with tunable in-plane anisotropy. *ACS Nano* **9,** 11249–11257 (2015).
50. Xia, F., Wang, H. & Jia, Y. Rediscovering black phosphorus as an anisotropic layered material for optoelectronics and electronics. *Nat. Commun.* **5,** 4458 (2014).
51. Cincotti, S. & Rabe, J. P. Self-assembled alkane monolayers on MoSe$_2$ and MoS$_2$. *Appl. Phys. Lett.* **62,** 3531 (1993).

Acknowledgements

We thank Wen Zhang and Joachim Räder for their help in the ASAP MS analysis. We acknowledge funding from the European Commission through the FET project UPGRADE (GA-309056), the Graphene Flagship (GA-696656), the Marie Sklodowska-Curie projects IEF GALACTIC (PIEF-GA-2014-628563) and ITN SYNCHRONICS (GA 643238), the Agence Nationale de la Recherche through the Labex projects CSC (ANR-10-LABX-0026 CSC) and Nanostructures in Interaction with their Environment (ANR-11-LABX-0058 NIE) within the Investissement d'Avenir programme (ANR-10-120 IDEX-0002-02), and the International Center for Frontier Research in Chemistry (icFRC). The work in Mons is supported by BELSPO through the PAI P6/27 Functional Supramolecular Systems project and the National Science Foundation for Research, FNRS. D.B. is an FNRS research director.

Author contributions

The experiment was conceived by M.G., S.B., P.S. and E.O.; M.G. performed the STM characterization and the device study; S.B. carried out the optical characterization and M.-A.S. the PESA measurements; M.A.S. and M.G. performed the C-AFM experiments.; J.X.L. performed the MD/MM/DFT and G.D. the microelectrostatic calculations under the supervision of Y.O. and D.B.; Y.L. and X.-Y.W. synthesized the molecules under the supervision of A.N., K.M. and X.F.; P.S. and E.O. supervised the entire study. M.G. wrote the manuscript with comments and suggestions from all co-authors.

Additional information

Supplementary Information accompanies this paper at http://www.nature.com/naturecommunications

Competing financial interests: The authors declare no competing financial interests.

Reprints and permission information is available online at http://npg.nature.com/reprintsandpermissions/

How to cite this article: Gobbi, M. *et al.* Periodic potentials in hybrid van der Waals heterostructures formed by supramolecular lattices on graphene. *Nat. Commun.* **8,** 14767 doi: 10.1038/ncomms14767 (2017).

Publisher's note: Springer Nature remains neutral with regard to jurisdictional claims in published maps and institutional affiliations.

Supplementary Figures

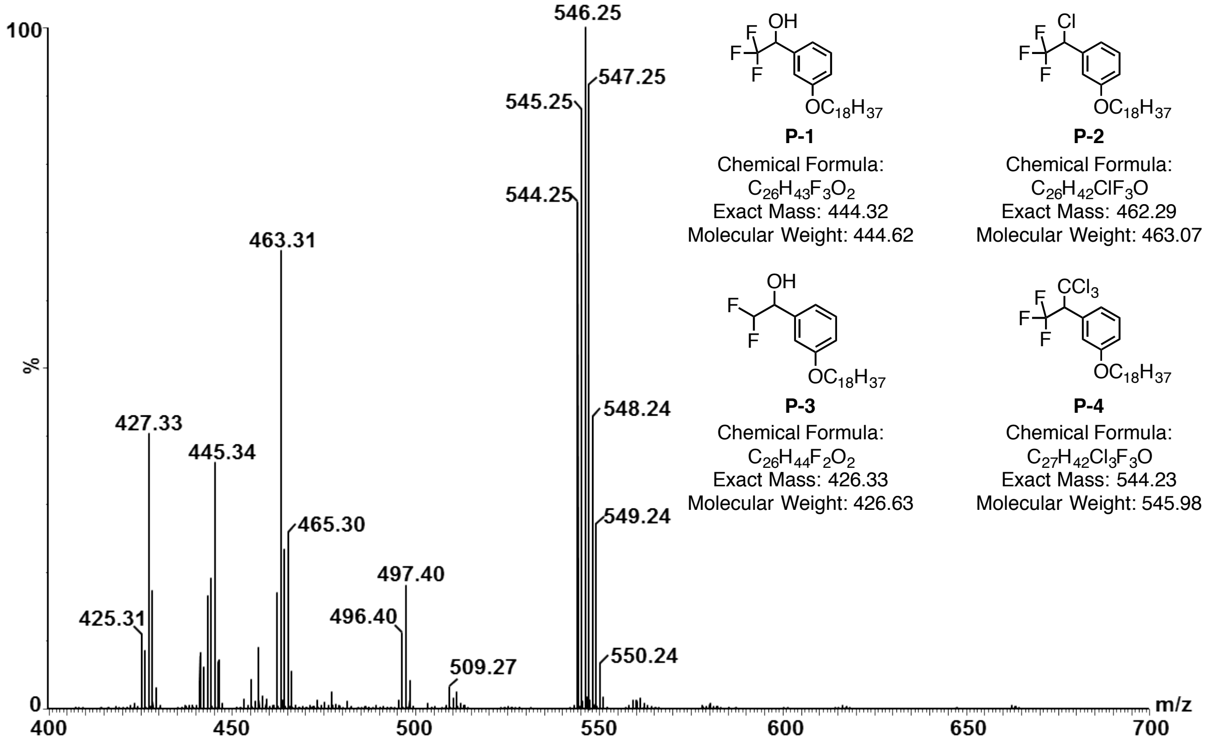

Supplementary Figure 1. Determination of the reaction products in MBB-2: Mass spectrometry. While MBB-1 is the unreacted pure compound, 3-trifluoromethyl-3-(3-octadecyloxyphenyl)diazirine, which is selectively synthesized, MBB-2 is a mixture of reaction products obtained by irradiation of MBB-1 with ultraviolet light at 365 nm in chloroform. The atmospheric solids analysis probe (ASAP) mass spectrometry (MS) analyses of the MBB-2 mixture shown in this Figure indicates the presence of a number of reaction products, including the derivatives called P-1 to P-4, displayed in inset. In the main reaction products, the 3-octadecyloxyphenyl group is maintained while the head is functionalized with another functional group such as hydroxy, chloro, or trichloromethyl.

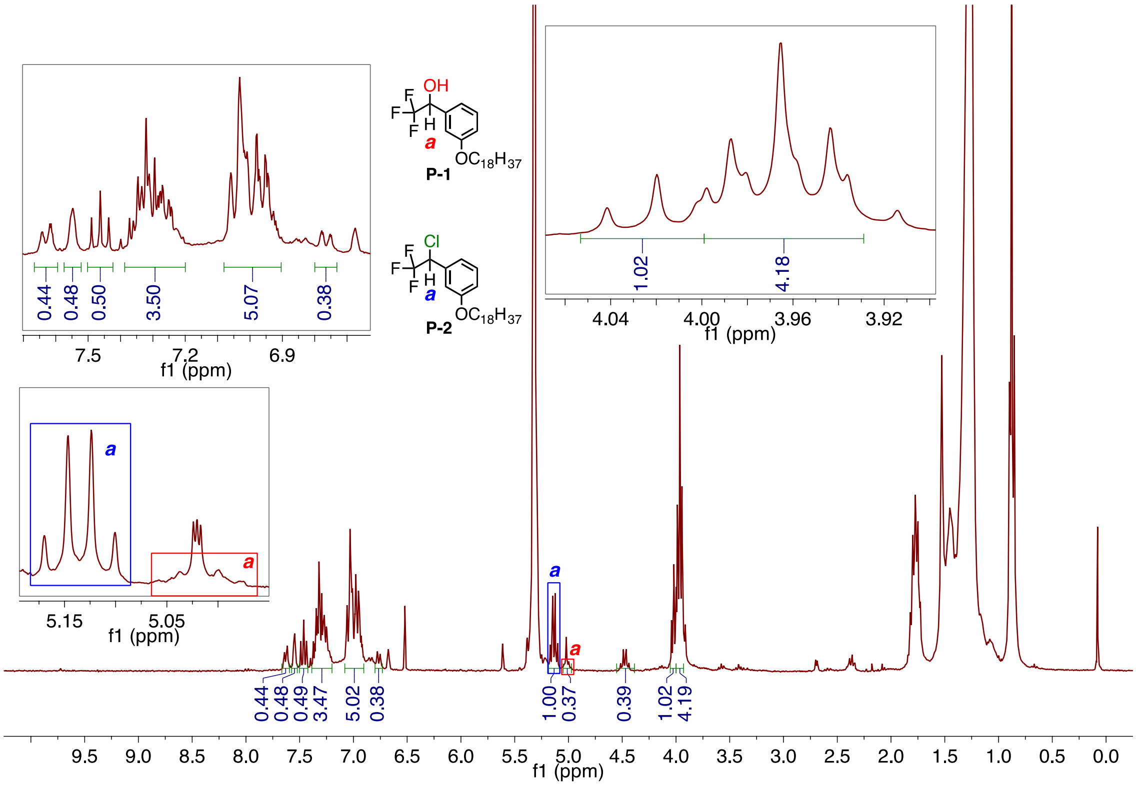

Supplementary Figure 2. Determination of the reaction products in MBB-2: Nuclear Magnetic Resonance spectroscopy. ^{1}H nuclear magnetic resonance (NMR) spectroscopy analysis of MBB-2, i.e., the reaction products from the photolysis of the diazirine derivative in chloroform (300 MHz, CD_2Cl_2). The ^{1}H NMR spectrum shows complex multiplet signals in the aromatic region as well as at 3.9–4.1 ppm, corresponding to the alkoxy protons -OCH_2-, which confirms the presence of different reaction products in agreement with the ASAP MS spectrum in Supplementary Figure 1. Based on the ^{1}H NMR spectra of separately synthesized P-1 and P-2, (Supplementary Figure 3), the quartet peaks centered at 5.01 and 5.13 ppm can be assigned to P-1 and P-2, respectively, as indicated by "*a*" and rectangles in red and blue colors. Considering the ratio of integration of these quartet peaks as well as the total integration of the triplet peaks from -OCH_2- at around 4 ppm as well as the aromatic signals, P-2 can be concluded to be the main component of the MBB-2 mixture. The blue numbers below the spectrum denote the integration of the peaks over the areas indicated by the green bars.

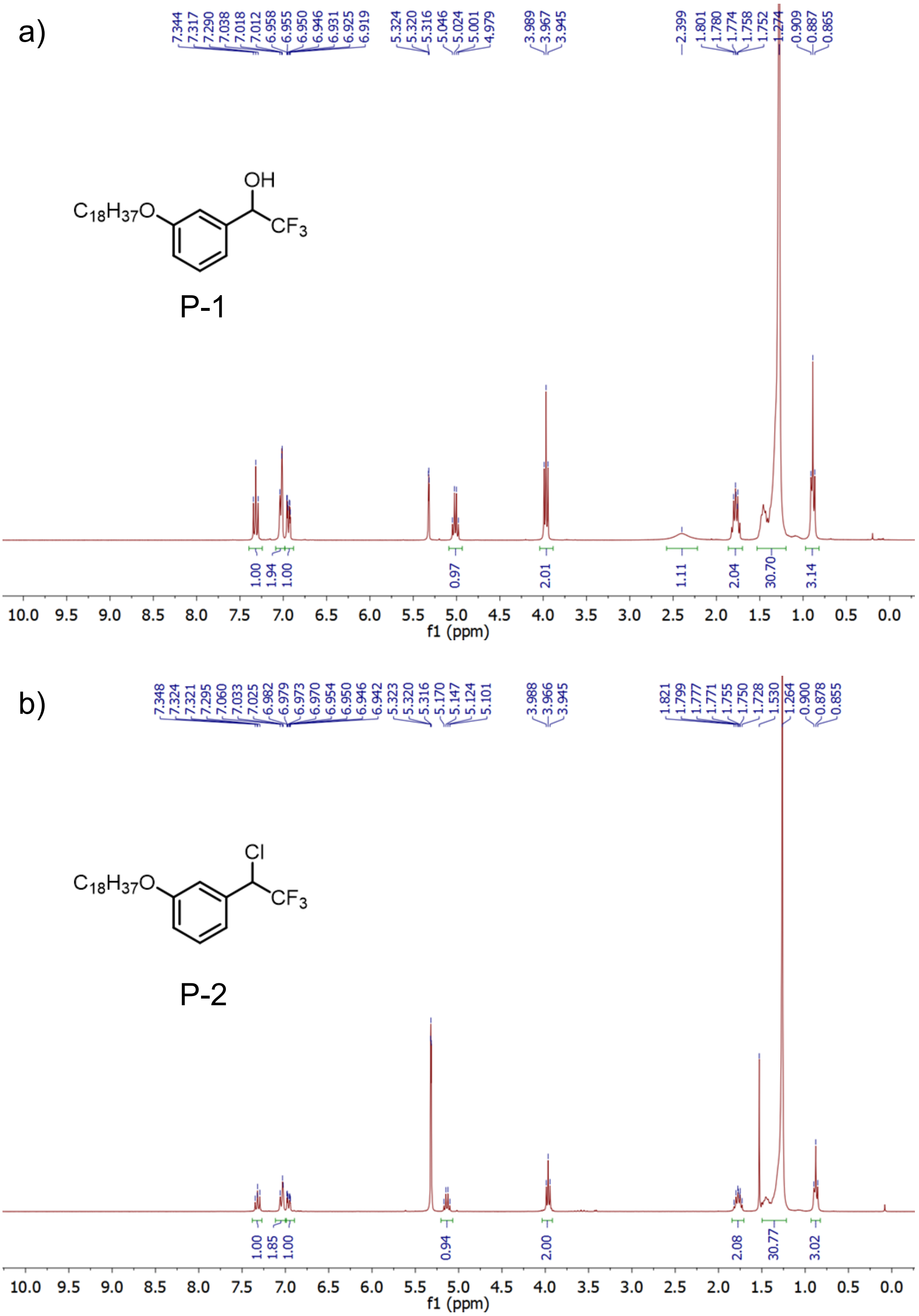

Supplementary Figure 3. ^{1}H NMR spectra of separately synthesized P-1 and P-2. The comparison of the ^{1}H NMR spectra (300 MHz, CD_2Cl_2) of the separately synthesized P-1 (a) and P-2 (b) with that of MBB-2 from the photoreaction (Supplementary Figure 2) confirmed the formation of P-1 and P-2 upon the photolysis of MBB-1 in chloroform (see the caption of Supplementary Figure 2).

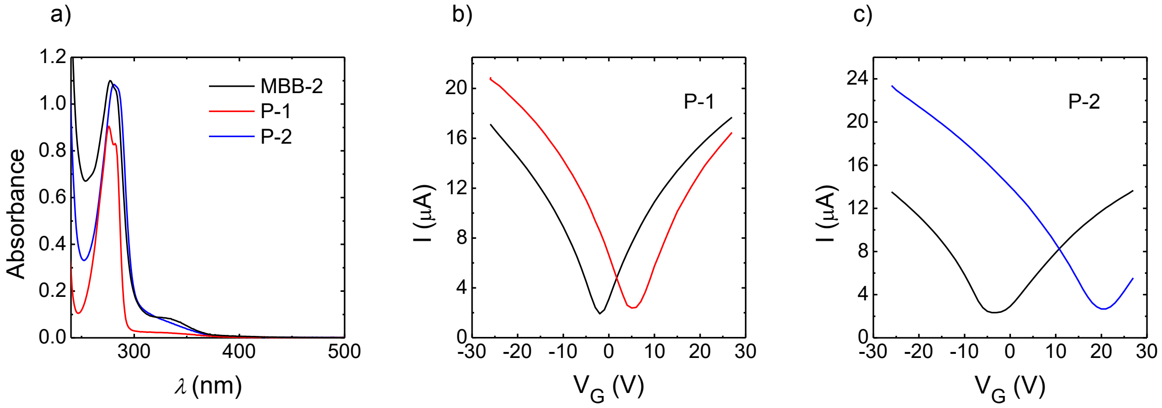

Supplementary Figure 4. Comparison between the mixture MBB-2 and the separately synthesized P-1 and P-2. (a) Comparison of the Ultraviolet (UV)-Visible spectra of the separately synthesized P-1 and P-2 and MBB-2, obtained by irradiating MBB-1 with UV light (concentration of P-1, P-2, MBB-1 2.2 $\times 10^{-3}$ M in chloroform; 2-mm quartz cells; room temperature). The UV-Visible spectra of the irradiated compound MBB-2 is remarkably similar to that of the Cl-modified P-2, confirming that this compound is the main reaction product. (b) Effect of the presence of hydroxyl-modified derivative P-1 on the electrical characteristics of graphene. Black line: pristine graphene device; red line: graphene device covered by a P-1 supramolecular lattice. (c) Effect of the presence of chloro-modified derivative P-2 on the electrical characteristics of graphene. Black line: pristine graphene device; blue line: graphene device covered by a P-2 supramolecular lattice. I is the current flowing through graphene, and V_G is the gate voltage.

As compared to the effect of MBB-2 (Fig. 3b), a significantly lower p-doping was introduced by P-1 (b). Instead, the effect of P-2 (c) is analogous to that of MBB-2. This finding strongly indicates that this compound is the main reaction product on the graphene surface after UV irradiation of the diazirine derivative in $CHCl_3$.

Following this findings, for the simulation of the effect of MBB-2, we assumed that all the molecules on the surface possess the P-2 structure. Although the presence of other reaction products at the surface cannot be fully ruled out, it would be a minor effect which does not change significantly the scientific outcome of this work.

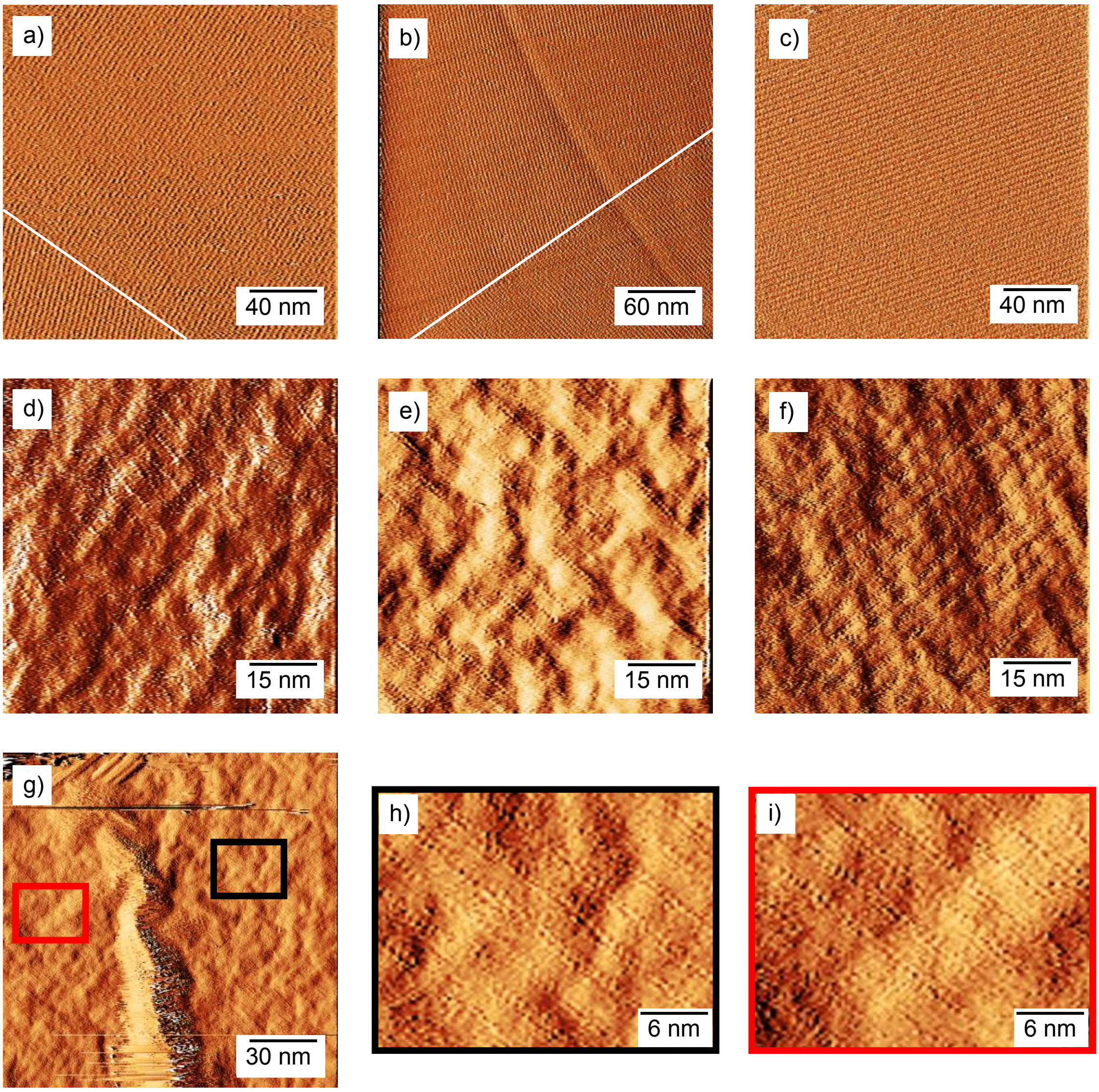

Supplementary Figure 5. Large area STM image of the supramolecular lattices. (a) MBB-1, (b) MBB-2, and (c) MBB-3 on highly oriented pyrolytic graphite. In (b) and (c), two domains with different orientation of the lamellas are visualized, and the domain boundary is highlighted by a white line. (d), (e), (f) STM image of the assembly of (d) MBB-1, (e) MBB-2, and (f) MBB-3 on graphene grown by chemical vapor deposition (CVD) and transferred on a SiO_2 substrate. In the three images, the direction of the lamella is maintained within the whole image. (g) Large area (150 nm × 150 nm) STM image of a single domain of MBB-2 spin-coated on CVD graphene on SiO_2. (h)-(i) Zoom-in of the two regions highlighted in (g), showing that the same direction of the assembly is kept on both sides of the central ripple. Typical tunnelling parameters: tip voltage (V_t) = 400-600 mV, and average tunnelling current (I_t) = 20-50 pA.

We highlight that the images of MBB-2 show a very uniform assembly, suggesting that mostly one compound is lying on the surface. Moreover, the similarity between the unit cells measured for MBB-1 and MBB-2 indicates that the size of the main reaction product is very similar in both cases, ruling out the bigger derivative P-4 as main product on the surface.

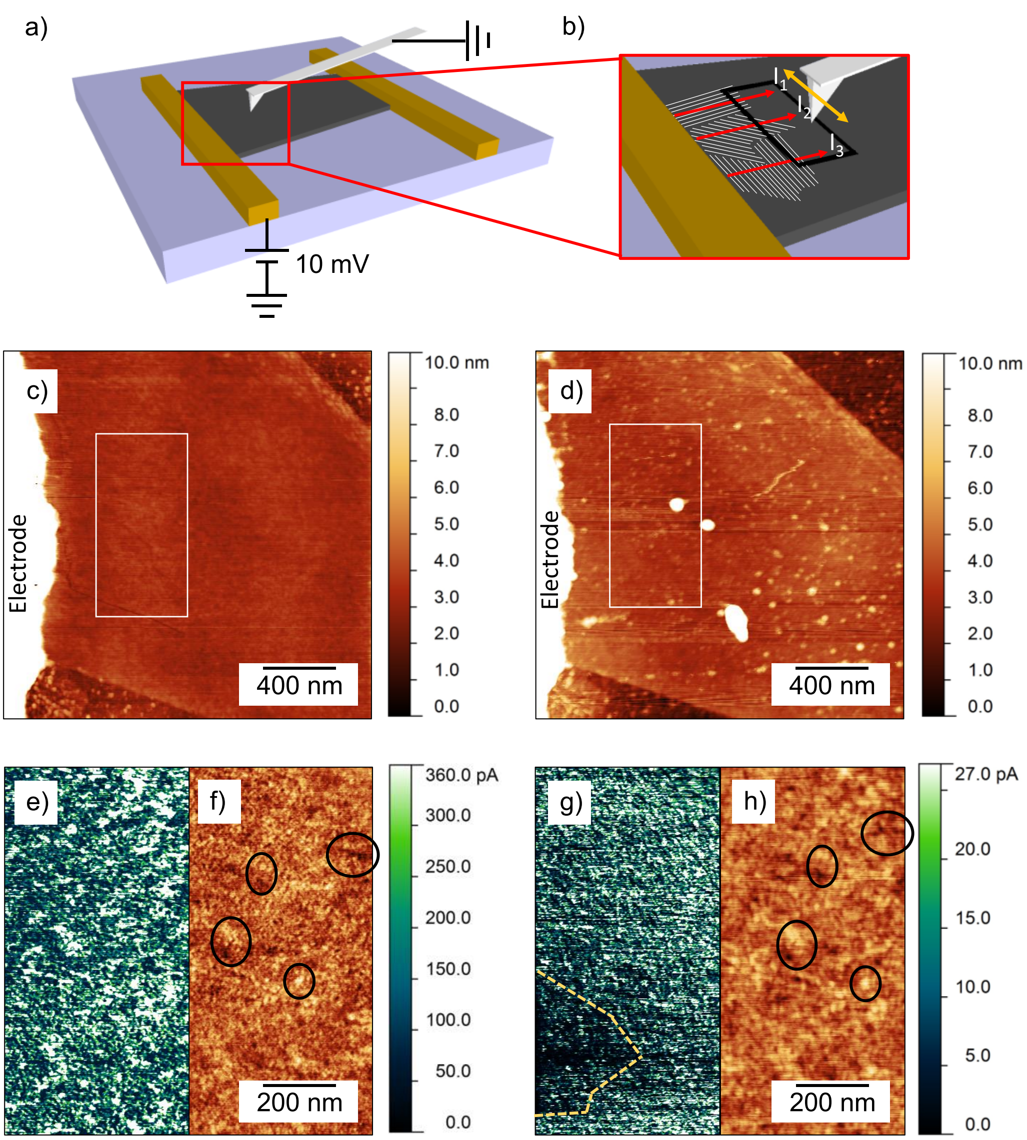

Supplementary Figure 6. Spatially-resolved current distribution. Conductive atomic force microscope (C-AFM) experiments were performed in the same area of the same graphene device before and after the formation of a supramolecular Lattice (SL) of MBB-1**.** (a) Schematic of the measurement. A conductive tip is scanned over the sample while a bias $V = 10$ mV is applied between the tip and a gold electrode, allowing to simultaneously measure morphology and current. (b) Cartoon of the effect of domain with different lamella orientation. The white lines represent SL domains with different lamella orientation while the black rectangle represents the scan area. I_1, I_2 and I_3 are the currents flowing across the SL/graphene area covered by SL domains with different lamella orientation. Owing to the anisotropy on graphene conductivity induced by the presence of the SL, the current reaching the tip depends on the local lamella orientation between electrode and tip. In a current map, this effect would be recorded as a spatial modulation of the current, with a length-scale comparable to that of single SL domains ($I_1 \neq I_2 \neq I_3$). (c, d) Morphology images of the graphene device at relatively large scale (2 × 2 μm^2) before (c) and after (d) the SL formation. The pristine graphene is extremely clean (c). After the SL formation, we found that the same area was covered with a molecular adlayer (d). The morphology of such layer is different from that of pristine graphene because a few protrusions, separated by flat regions, could be imaged by AFM. Such flat regions as areas in which graphene is covered strictly by one monolayer, and the protrusions as 3D molecular aggregates. We note that the electrical contacts do not impact significantly the order within the molecular layer; at the least, no evident material accumulation/depletion close to the contact is encountered. (e-h) Current and morphology maps measured before (e and f) and after (g and h) the SL formation, recorded in the smaller region of the device in the areas highlighted in (c) and (d), at a distance approximately 200 nm from the electrode. Such distance is shorter than the typical size of a SL single domain, so it can be assumed that only one or at most two SL domains are comprised between the electrode and the closer side of the image. By comparing morphology images recorded before and after the SL formation (f and h), one can univocally recognize the same surface features (some of which are indicated by the black circles), confirming that the images were recorded in the very same area. The lamella orientation could not be resolved, most probably since the 3.8-nm stacking is below the resolution limit of the C-AFM.

Noteworthy, the current images measured before and after the SL are significantly different. The current map measured for the pristine device (e) displays a short-range modulation with a typical length scale of a few tens of nm^2, which follows the graphene roughness, as can be noticed by comparing the current map (e) and morphology image (f), recorded simultaneously. Such short-range current modulation can be ascribed to the tip-graphene contact that locally varies owing to graphene roughness that affects the current injection locally. The current map measured after the SL formation (g) displays two main differences as compared to the pristine case: (1) the current averaged over the whole image is more than one order of magnitude lower (I_{after} = 14 pA vs I_{before} = 250 pA) and (2) the current is inhomogeneous on a length scale of a few-hundreds nm^2. The lower average current can be explained considering that the presence of the insulating molecular layer on the surface of graphene increases the overall resistance of the system, and that after the SL formation we recorded the image applying a lower force between the tip and the sample (2 nN before and 1.5 nN after the SL formation), in order to minimize the removal of molecules by the tip. More interestingly, we found that the presence of the SL introduces inhomogeneities in the conductance of graphene. In particular, we observe a region of a few hundred nm^2 with markedly lower current, delimited by the yellow dotted guide to the eye in panel (g). The average current measured within this region is one third of the average current outside of it (5 pA vs. 15 pA). In (h) there are no features which could explain the lower current measured in such region. A very similar current map was obtained by scanning the same region with the fast scan direction either parallel or perpendicular to the electrical contact, ruling out possible artefacts related to tip deterioration during the imaging. The size of the low-conductance region (few hundred nm^2) roughly matches that of single crystalline domains of the SL. As explained above, this experimental evidence supports the presence of anisotropic conductance within graphene areas covered by SLs with random local lamella orientation.

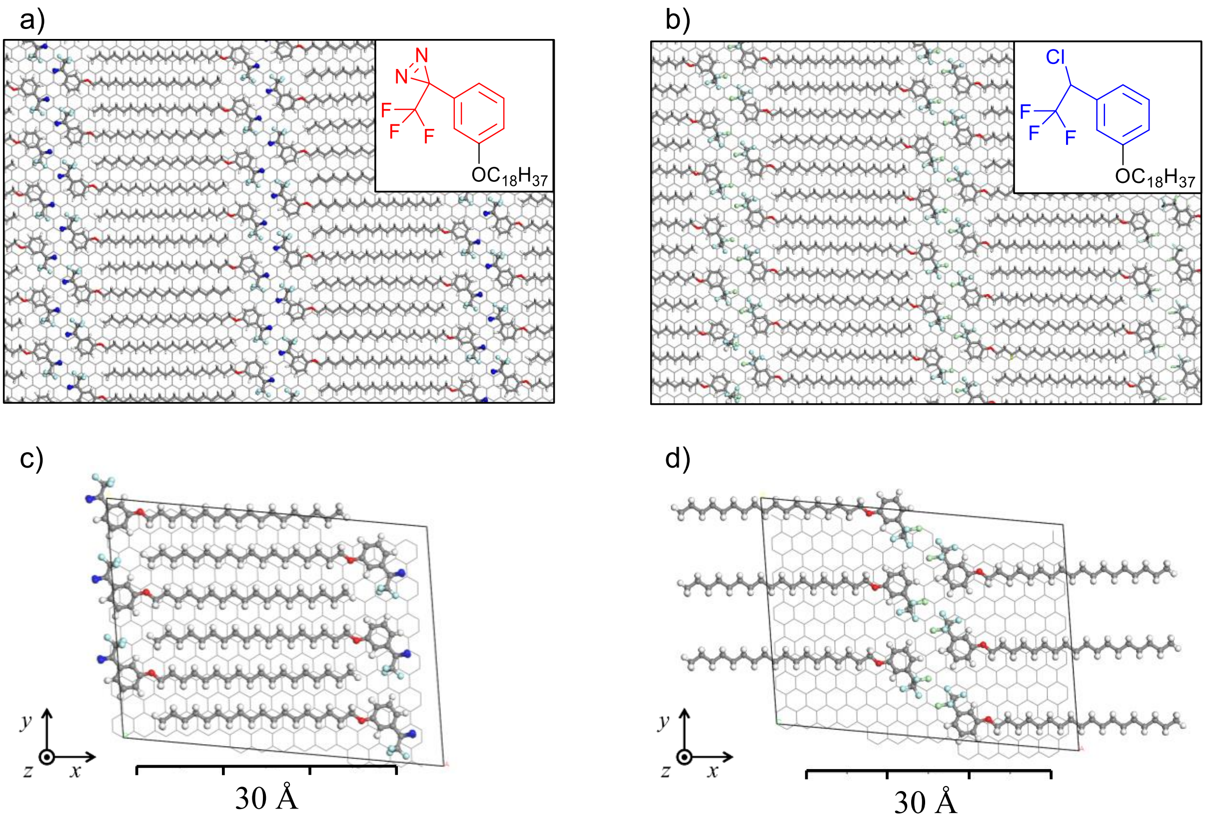

Supplementary Figure 7. Assemblies and unit cells predicted *via* molecular dynamics simulations. (a,b) Predicted assemblies for MBB-1 (a) and MBB-2 (b). Insets: molecular structures of MBB-1 and MBB-2. (c,d) Unit cells for MBB-1 (c) and MBB-2 (d).

The force field molecular dynamics simulations show that both the MBB-1 and MBB-2 are packed in a lamellar structure with head-to-head configuration. For both molecular adlayers, the smallest repeating motives (c,d) of the supramolecular lattice have been carefully extracted accounting for the atomic positions of the diazirine derivatives relative to the carbon atoms of the underlying graphene. In these unit cells, six molecules (i.e., three dimers) are required for a reasonable commensuration of the molecular adlayers with the graphene surface. Thus, the calculated lattice parameters of the unit cell are: $a \approx 3.7$ nm, $b \approx 2.8$ nm (area ≈ 10.2 nm²) and $\alpha \approx 81°$. We note that the calculated unit cell parameters were found for both MBB-1 and MBB-2, and are in very good agreement with the experimental data (see main text). The energy minimization of the supramolecular lattice/graphene systems was performed in vacuum, under periodic boundary condition (PBC), and carried out using the Conjugate-Gradient algorithm, until the RMS force was less than 5×10^{-3} kcal mol^{-1} Å with energy convergence of 1×10^{-4} kcal mol^{-1} between steps. Series of 25-ps-quenched dynamics (T = 50,100, …, 300 K, quench frequency = 1 ps) for which different temperatures were used so that the energy between quenched dynamics would no longer decrease. The molecular dynamics simulations were conducted in the NVT ensemble, using the Nosé thermostat.

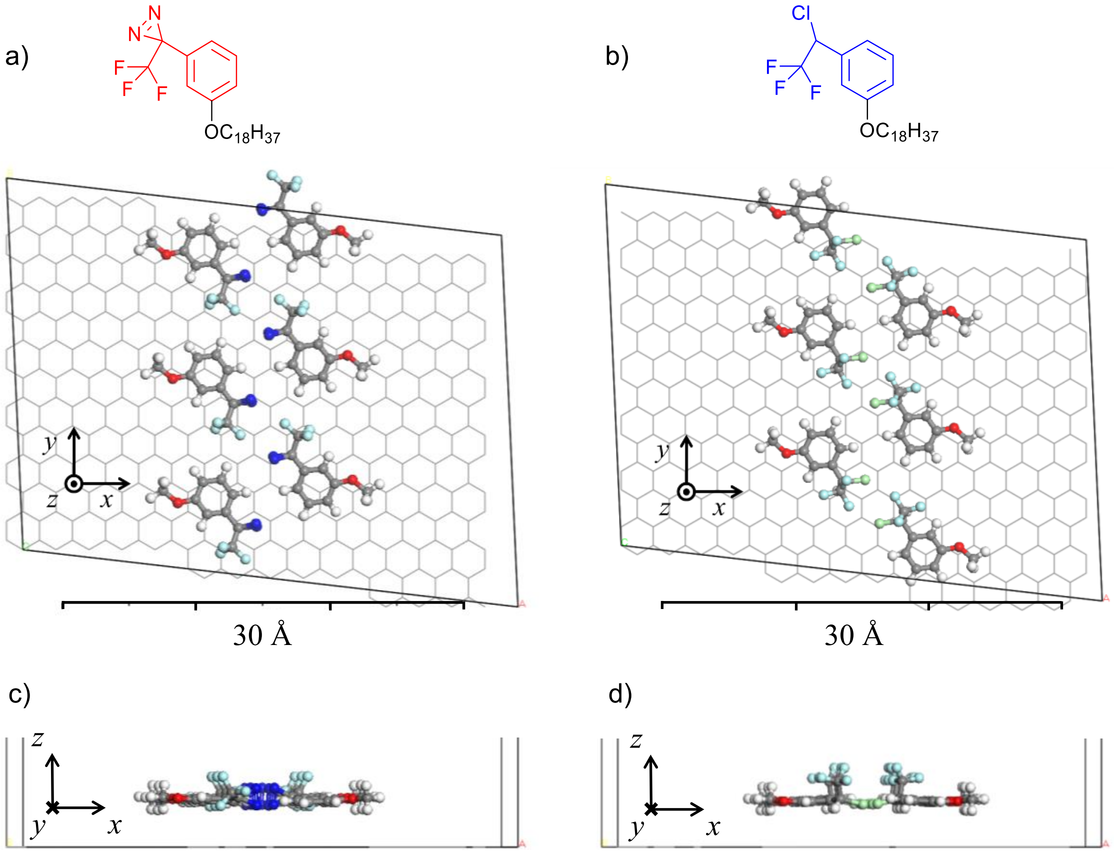

Supplementary Figure 8. Unit cells used in the density functional theory calculations. (a) Top view and (c) side view of the unit cell used in the density functional theory (DFT) calculations for MBB-1. (b) Top view and (d) side view of the unit cell used in the DFT calculations for MBB-1. Using these unit cells, DFT calculations were performed to evaluate the charge density redistribution as well as the influence of the electrostatic potential induced by the supramolecular lattices on the work function of graphene. The atomic positions have been optimized at the molecular mechanics/molecular dynamics level, while no optimization of the unit cell has been performed at the DFT level. In order to considerably reduce the computation time, the linear alkyl chains were removed, i.e., $C_{21}H_{43}$ groups were substituted by CH_3 groups. Indeed, the saturated chains should not contribute to the doping of graphene. Thus, the unit cells consist in a graphene layer of 388 carbon atoms and 6 (MBB-1 or MBB-2) moieties on top of it.

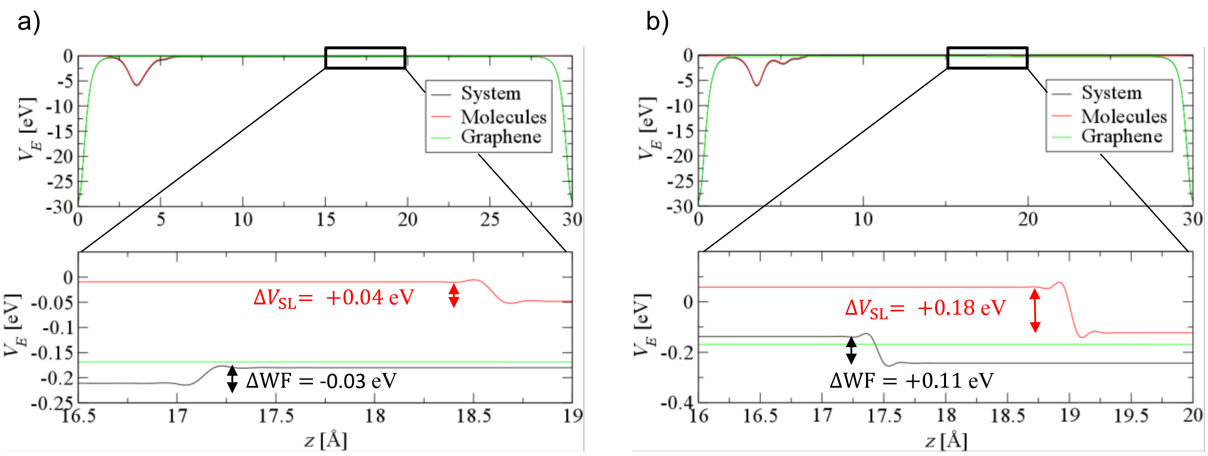

Supplementary Figure 9. Potential profile at the graphene/supramolecular lattice interface from density functional theory. (a) Profile of the potential V_E across the graphene/MBB-1 interface; (b) Potential profile across graphene/MBB-2 interface (*z*-direction normal to the graphene surface). (c), (d) Zoom on the vacuum level shift (far from the interface). Black line: potential of the entire system composed of graphene + supramolecular lattice (SL), related to the change in work function ΔWF. Red line: potential of the isolated SL, the variation of which will be called ΔV_{SL}. Green line: potential related to the charge transfer contribution to graphene ΔV_E.

The plane-averaged electrostatic potential *V*(z) was calculated numerically from the self-consistent SIESTA potential *V*(*x*,*y*,*z*) using the macroscopic average technique developed by Baldereschi et al. [1]

Following the methodology described in Supplementary Methods, to distinguish the contributions to the work function shift ΔWF (intrinsic dipole moment of the SL ΔV_{SL} and charge transfer ΔV_E), we analysed the potential profile of the full supramolecular lattice (SL)-graphene system and the isolated SL. In the case of MBB-1, the decomposition shows that the contribution of the SL (ΔV_{SL}= +0.04 eV) is compensated by the charge transfer term (ΔV_E = -0.07 eV), leading to a relatively weak decrease of work function (ΔWF = -0.03 eV). In the case of MBB-2, ΔV_{SL} and ΔV_E are opposite in sign, meaning their effects partly cancel out, yet the net effect is a WF shift of approximately 0.10 eV. Such a work function shift is indicative of a p-type doping, which is in line with experimental observations. Interestingly, it is found that the energy term associated to the charge transfer is identical in the two cases (approximately ΔV_E = -0.07 eV). This indicates that ΔWF for MBB-2 mainly results from the modification of the intrinsic dipole moment of the SLs.

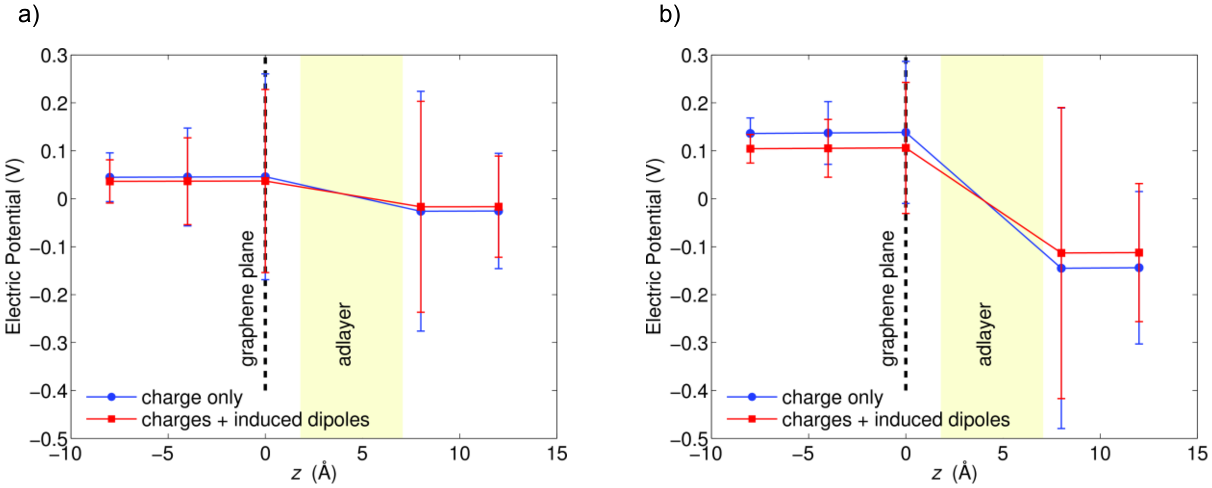

Supplementary Figure 10. **Potential profile at the graphene/supramolecular lattice interface from microelectrostatic calculations.** (a) Calculations for MBB-1 and (b) for MBB-2 supramolecular lattices adsorbed on graphene. As compared to Supplementary Figure 9, the potential profile shown in this picture is analogous to the contribution in the work function shift due to the presence of the molecular electrical dipoles ΔV_{SL}.

Symbols and error bars show the average and standard deviation of the potential in planes at different distances from the $z = 0$ graphene plane. Circles and squares show the potential profile obtained with the gas-phase molecular charge distribution, approximated by atomic charges from electrostatic potential fitting (charge only), and accounting for molecular polarizability (charges + induced dipoles). The potential step across the plane reduces from 0.28 eV to 0.22 eV when the polarizability of the MBB-2 adlayer is accounted for, whereas the change is negligible when polarizability of the MBB-1 is considered.

The presence of the organic adlayer induces a change in the electrostatic potential when crossing the graphene plane, and the potential step corresponding to MBB-2 is four times larger than that of MBB-1. In particular, the polar CF_3 groups pointing their more electronegative fluorine atoms away from the surface result in an electrostatic potential that is shifted to large negative values on top of the aromatic cores, while smaller positive values are computed on top of the alkyl chains. Overall, the microelectrostatic (ME) calculations indicate a shift in the potential consistent with p-doping of the graphene layer, in quantitative agreement with the DFT results ($\Delta V_{\mathrm{SL}} = 0.18$ eV from DFT against approximately 0.2 eV from ME, calculated for MBB-2 (b).

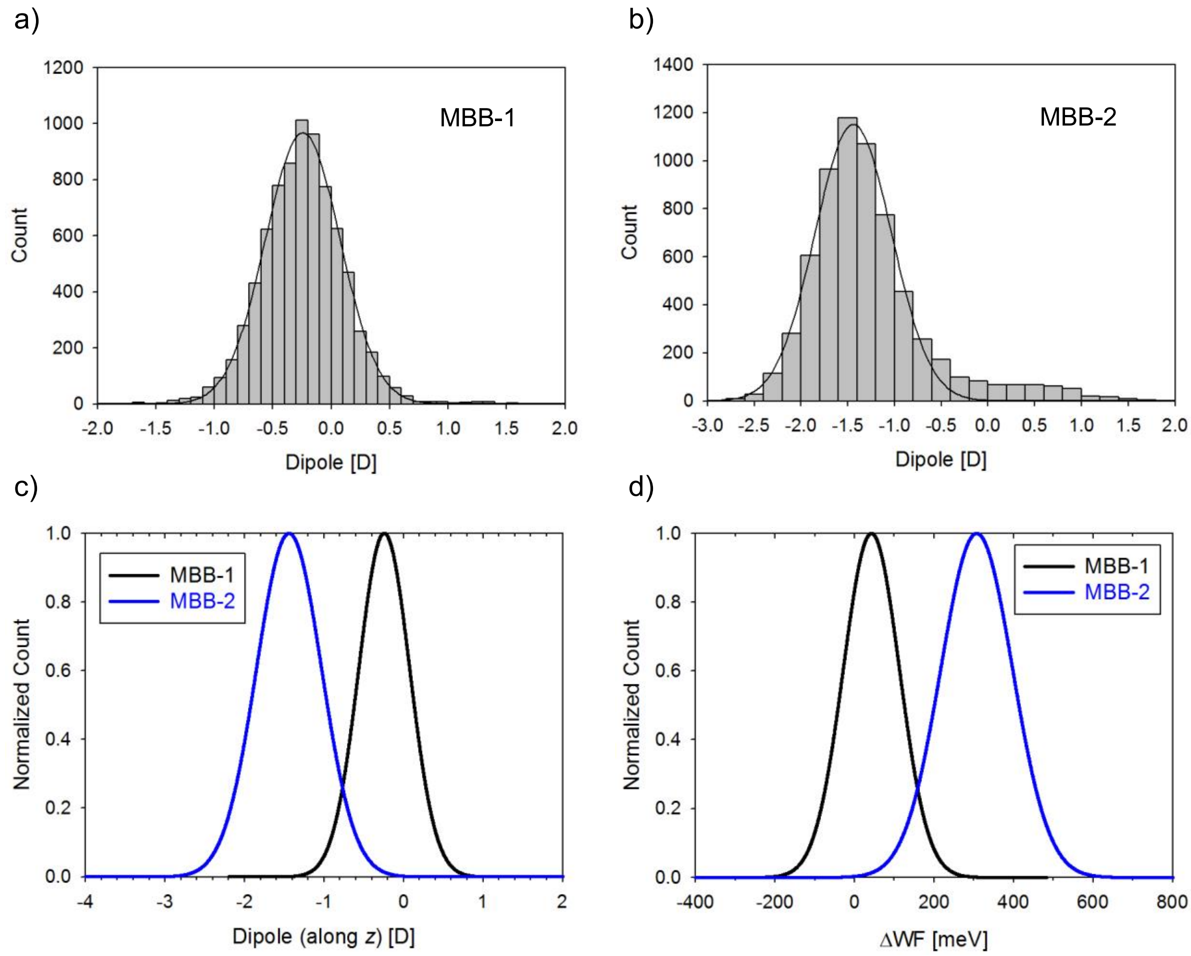

Supplementary Figure 11. Thermal distribution of molecular dipoles within the assembly and correspondent distribution of work function shift. (a,b) Thermally-smeared distribution of electrical dipoles calculated by molecular dynamics (MD) for MBB-1 (a) and MBB-2 (b). (c) Comparison of the fits to the electrical dipole distribution for MBB-1 and MBB-2, as extracted by (a) and (b). (d) Corresponding work function distribution for MBB-1 and MBB-2.

At room temperature, the supramolecular lattices undergo thermal vibrations and, therefore, the molecules can explore multiple configurations at the graphene surface. In turn, the different configurations are characterized by different orientation of molecular dipoles, which determine different work function shifts (ΔWF). To build a distribution of the molecular dipoles, we first performed MD simulations on the SL-graphene systems previously calculated (from which the unit cells were extracted). A molecular dynamics simulation of 100 ps was then performed and the electric dipoles of the molecules in the supramolecular lattice were recorded every 1 ps (100 frames). Next, we analyzed the correlation between the direction of the dipole moment and the geometry of the diazirine moiety on the graphene surface. For the MBB-1 derivative, we found a single population in which the molecule is flat on the graphene surface with the CF_3 group oriented in plane (Figure 3c and 3d in the main text). As shown in (a), the MD-calculated electric dipoles follow a Normal distribution, ranging from -1.5 to 1 D, with an average value and standard deviation of -0.2 and 0.3 D, respectively. In the case of MBB-2, a single population of electric dipole is also observed, yet now the Normal distribution is centered at -1.4 D with a standard deviation of 0.4 D (b). The geometry associated to this dipole distribution is shown in Figure 3d in the main text. As detailed in Supplementary Methods, we calculated a distribution of ΔWF (including a fixed ΔV_E contribution) for each dipole configuration for MBB-1 and MBB-2. The results reported in (d) have been renormalized per molecule (by dividing the surface by the number of molecules in the unit cell). The average and the standard deviation of the ΔWF distribution are 0.04 eV and 0.071 eV (0.31 eV and 0.09 eV) for the MBB-1 (MBB-2) derivative, respectively. Therefore, when the thermal vibrations are taken into account the ΔWF for MBB-2 increases to 0.31 eV from the 0.10 eV calculated at the density functional theory (DFT) level, indicating a strong p-doping in line with the experimental findings. Instead, the MD calculated ΔWF associated to MBB-1 has a sign opposite to that calculated at the DFT level. Yet, the main effect is weak in both cases, with differences arising from the neglect of depolarization effects in the MD simulations or of thermal effects in the DFT calculations.

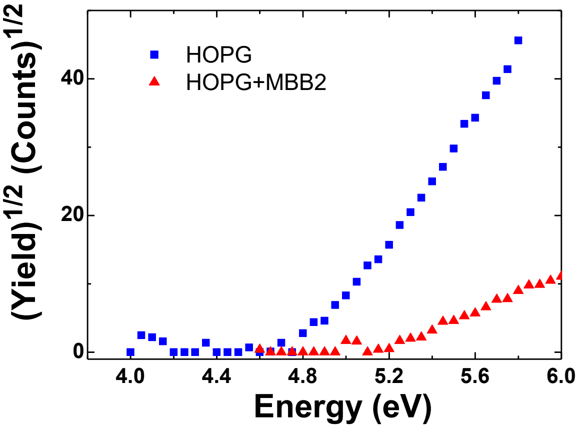

Supplementary Figure 12. Measurement of the work function shift through photoelectron spectroscopy in air. Representative measurements of the work function (identified by the intercept of the linear fitting of the curve with the Energy axis) for a freshly-cleaved highly oriented pyrolytic graphite HOPG sample and for the same surface after spin-coating MBB-2. The measurements were carried out by photoelectron spectroscopy in air (PESA) with an AC-2 Photoelectron Spectrometer (from Riken-Keiki Co.). The ultraviolet (UV) incident light power used for the measurements was 200 nW with a counting time of 10 seconds per point. As a substrate, we employed a 10 mm × 10 mm HOPG substrate, which can be cleaved to obtain clean surfaces. First, we took photoemission spectra in three different region (2 mm × 2 mm) of a freshly cleaved HOPG sample. Subsequently, we spin-coated MBB-2 on the same surface and repeat the measurements by probing different regions. A representative measurement before and after the SL formation is shown in Supplementary Figure 15. Averaging over ten samples, we obtained WF=4.85 ± 0.05 eV for the freshly cleaved HOPG surface and WF= 5.25 ± 0.15 eV for the HOPG surface covered by MBB-2. The work function shift ΔWF = 0.4 ± 0.2 eV is in good agreement with the theoretical calculations. We also highlight that a ΔWF = 0.3 eV shift in the graphene work function was found to correspond to a change in the induced charge density $\Delta p = 5 \cdot 10^{12}$ cm^{-2},[2–4] in excellent agreement with the experimental result for MBB-2 (see the main text).

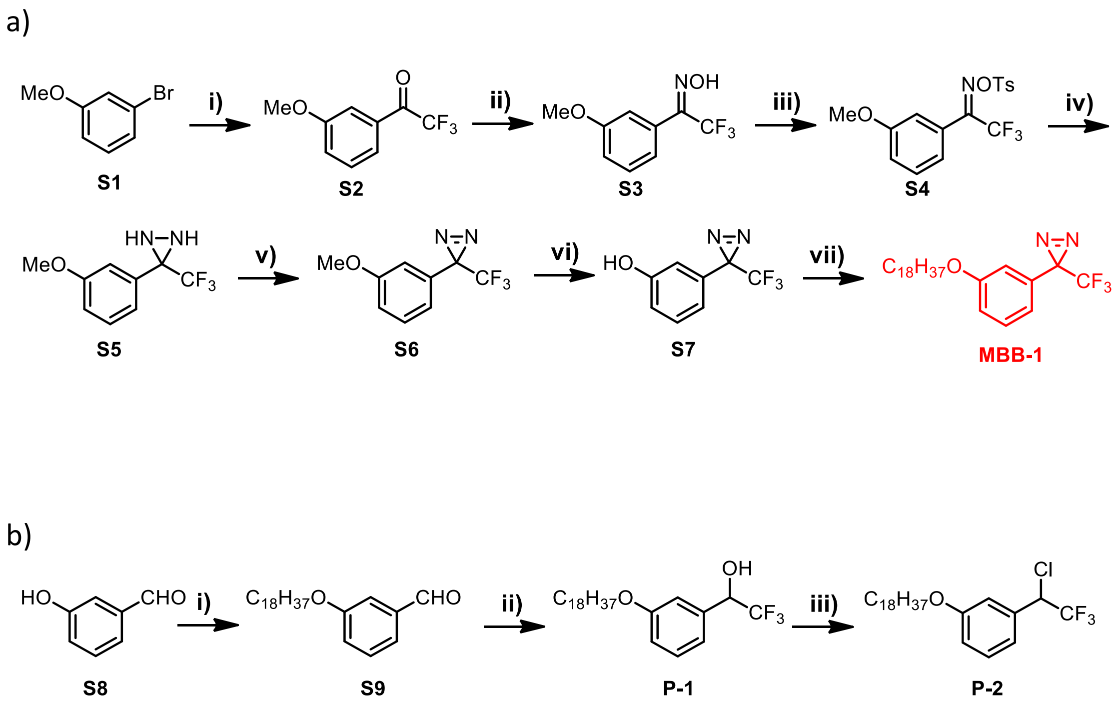

Supplementary Figure 13. Synthesis of MBB-1, P-1 and P-2. (a) Synthetic route to the molecular building block MBB-1 with a long alkoxy chain. The diazirine precursor 3-(3-(trifluoromethyl)-3*H*-diazirin-3-yl)phenol (S7) was synthesized according to the literature.[18] Reagents and conditions: i) *n*-BuLi, Et_2NCOCF_3, THF, –78 °C, 3 h; ii) NH_2OH-HCl, EtOH, 70 °C, 4 h; iii) TsCl, NEt_3, DMAP, DCM, RT, 24 h; iv) NH_3, DCM, –78 °C, 12 h; v) Ag_2O, Et_2O, RT, 20 h; vi) BBr_3, DCM, RT, 12 h; vii) $C_{18}H_{37}Br$, K_2CO_3, acetone, 60 °C, 65%. THF: tetrahydrofuran; Ts: *p*-toluenesulfonyl; DMAP: 4-dimethylaminopyridine; DCM: dichloromethane. (b) Synthetic route to P-1 and P-2**.** Reagents and conditions: i) $C_{18}H_{37}Br$, K_2CO_3, acetone, 60 °C, 89%; ii) $TMSCF_3$, K_2CO_3, DMF, RT, 12 h; then HCl (1.0 M, aq), RT, 1 h, 85%; iii) $SOCl_2$, pyridine, DMF (cat.), 80 °C, 63%. DMF: dimethylformamide. The detailed synthetic procedures and characterizations are described in Supplementary Note 1.

Supplementary Tables

<table>
<tr><th colspan="5">MBB-1</th></tr>
<tr><td>Image Size (nm^2)</td><td># images</td><td># images with single domain</td><td># images with two domains</td><td># images with three domains</td></tr>
<tr><td>60 × 60</td><td>6</td><td>5</td><td>1</td><td>0</td></tr>
<tr><td>80 × 80</td><td>4</td><td>2</td><td>2</td><td>0</td></tr>
<tr><td>90 × 90</td><td>1</td><td>0</td><td>1</td><td>0</td></tr>
<tr><td>100 × 100</td><td>2</td><td>1</td><td>1</td><td>0</td></tr>
<tr><td>200 × 200</td><td>1</td><td>1</td><td>0</td><td>0</td></tr>
<tr><td>300 × 300</td><td>1</td><td>0</td><td>1</td><td>0</td></tr>
<tr><th colspan="5">MBB-2</th></tr>
<tr><td>Image Size (nm^2)</td><td># images</td><td># images with single domain</td><td># images with two domains</td><td># images with three domains</td></tr>
<tr><td>60 × 60</td><td>5</td><td>3</td><td>2</td><td>0</td></tr>
<tr><td>80 × 80</td><td>1</td><td>0</td><td>1</td><td>0</td></tr>
<tr><td>90 × 90</td><td>1</td><td>0</td><td>1</td><td>0</td></tr>
<tr><td>100 × 100</td><td>3</td><td>2</td><td>1</td><td>0</td></tr>
<tr><td>150 × 150</td><td>2</td><td>2</td><td>0</td><td>0</td></tr>
<tr><td>200 × 200</td><td>3</td><td>0</td><td>2</td><td>1</td></tr>
<tr><th colspan="5">MBB-3</th></tr>
<tr><td>Image Size (nm^2)</td><td># images</td><td># images with single domain</td><td># images with two domains</td><td># images with three domains</td></tr>
<tr><td>60 × 60</td><td>4</td><td>3</td><td>1</td><td>0</td></tr>
<tr><td>100 × 100</td><td>2</td><td>1</td><td>1</td><td>0</td></tr>
<tr><td>200 × 200</td><td>1</td><td>1</td><td>0</td><td>0</td></tr>
</table>

Supplementary Table 1. Summary of large-area scanning tunnelling microscopy images recorded for MBB-1, MBB-2 and MBB-3. For each molecular building block (MBB), we recorded at least 80 STM images considering both highly oriented pyrolytic graphite and CVD graphene on SiO_2. For relatively small images (< 40 nm × 40 nm), we always observed a single domain in the image – corresponding to lamellas oriented in the same direction all over the image. Therefore, only relatively large images (> 60 nm × 60 nm) are relevant for an estimation of the average domain size. This table provides a detailed analysis of these images, highlighting the number of domains encountered on each large-scale image. Limiting the discussion to the relevant data (images size > 60 nm × 60 nm), we have measured 15 images for both MBB-1 and MBB-2, and 7 for MBB-3.The images were recorded in different STM sessions, on different samples (prepared in the same way). In the case of images recorded one after the other in the same spot, only the first one was taken into account. In all large-area images, either a single domain or two domains separated by a domain boundary are imaged (additional large-area STM images are shown in Supplementary Fig. 7). An entire domain would never be fully included into a single image, even on the largest scale. Hence, we conclude that single domains are typically wider than our maximum image size – typically 200 nm × 200 nm. The fact that a domain boundary is often imaged brings us to conclude that a reasonable value for the typical domain size is 300 × 300 nm.

	μ_x [D]	**μ_y** [D]	**μ_z** [D]	**ΔV_{SL}** [eV]	**ΔV_E** [eV]	**ΔWF** [eV]	**Doping**
MBB-1	0.01	0.00	-0.17	+0.04	-0.07	-0.03	n
MBB-2	0.03	0.01	-0.82	+0.18	-0.08	+0.10	p

Supplementary Table 2. Molecular dipoles and variation of the work function of graphene upon physisorption of different supramolecular lattices. The electric dipole per molecule along the three direction μ_x, μ_y, μ_z are expressed in Debye, while the contribution to the electrostatic potential associated to the intrinsic dipole moments of self-assembled monolayers (ΔV_{SL}) and to charge transfer (ΔV_{E}) as well as the resulting work function shift (ΔWF) are in electronvolt. The resulting doping type is also indicated. As detailed in Supplementary Methods, the molecular dipoles have been calculated by molecular dynamics simulations, while the variations in the surface potential by Density Functional Theory. Since ΔV_{E} is analogous in both cases, the difference in ΔWF can be ascribed mostly to the different vertical dipoles μ_z.

F is a strongly electron-withdrawing atom, so one would expect F-rich molecules to induce strong charge transfer. Indeed, molecules such F_2-HCNQ[5] and F_4-TCNQ[2] are known to be efficient dopants for graphene. All compounds encompassed within our study comprise a -CF_3 group which could be thought of as a source of electron extraction from graphene as well. However, this was not found to be the case in our study, as evidenced by the relatively weak ΔV_{E} for MBB-1 and MBB-2. Actually, in order to obtain efficient charge transfer, the molecular levels should lie close to the Fermi level of graphene. When that is the case, an electron flow can take place from or to graphene to reach equilibrium, possibly mediated by partial molecule-graphene hybridization and the formation of interfacial states acting as scattering or trapping centers[6]. The fact that fluorinated molecules are often used as dopants is due to the fact that very often in conjugated molecules the presence of withdrawing electron groups (F atoms) lowers the LUMO and brings it closer to the Fermi level of graphene. Instead, in our system, the LUMO level of the molecule lies far in energy from the Fermi level of graphene, thus preventing efficient charge transfer. Indeed, we calculated the frontier orbitals of a methoxy-trifluoromethyl-phenyl-diazirine in chloroform at the B3LYP level (see Supplementary Methods). The LUMO lies at -2.34 eV, which is more than 2 eV higher than the Fermi level of graphene (-4.6 eV).[7] Moreover, it has been reported recently that the effect of dielectric fluoro polymers on the graphene characteristics is very similar to what is reported here for MBB-1: minor overall doping, with an increase in the graphene mobility.[8] In conclusion, it is not generally true that F-rich molecules withdraw electrons, and in particular MBB-1 and MBB-2 introduce minor charge transfer. Instead, their doping effect measured is mediated by the presence of aligned out-of-plane molecular dipoles, as shown by our calculations.

Supplementary Methods

Methodology for the modeling. The formation of a MBB-1 supramolecular lattice (SL) is investigated by molecular mechanics/dynamics (MM/MD) simulations. The change in the work function (WF) due to the photo-reaction of the diazirine molecules is analyzed using density functional theory (DFT) calculations. Following the above discussion, for the simulation of the effect of MBB-2, we assumed that all the molecules on the surface possess the P-2 structure. The doping is evaluated in terms of work function shift (ΔWF) of graphene in the presence of SL of MBBs. The procedure involves three successive steps: i) force field parameterization based on quantum-chemistry calculations; ii) MD simulations of the supramolecular 2D architectures and extraction of the unit cell from the optimized SL; and iii) DFT electronic structure calculations on the optimized unit cell. Note that the combination of (ii) and (iii) allows converting the MD distribution of the molecular conformation and electric dipole of the individual diazirine molecules into WF distributions.

Force field parameterization. An all-atom description was used for the individual molecules, i.e., all hydrogen atoms were taken into account. For the aliphatic chains of the molecules, the COMPASS force field (FF) was used for all the atomic charges, except for the first $–CH_2–$ unit close to the MC functional group. For the latter, the atom types were described at the quantum chemistry level, with atomic charges calculated from the electrostatic potential (ESP charges)[9] on the basis of MP2/cc-pvdz optimized geometry, as implemented in the Gaussian09 package.[10i] Then chemically equivalent atoms were set with equal (averaged) charges. To describe the phenyl-CF_3 torsional potential at the Molecular Mechanics level of theory, the Dreiding force-field was re-parameterized against reference MP2/cc-pvdz torsional potentials. All MM/MD calculations were performed with the Materials Studio 6.0 package using our fine-tuned Dreiding force-field.

Molecular dynamics simulation details and unit cell extraction. Prior to the construction of the SLs, preliminary MD calculations were run in order to determine the relative stability of different orientations of the molecules with respect to the graphene layer, and between molecules (the relative orientations and shifts of the functional groups and alkyl chains, the inter-digitation of the alkyl chains, etc.). The SLs of MBB-1 or MBB-2 were built atop the graphene surface, which consists in a layer of 14400 carbon atoms (222 × 170 Å^2); the graphene layer was spatially frozen, as its geometry is expected to be weakly perturbed upon physisorption of the molecules. Four stacks of 16 (i.e., 64) molecules were initially placed at ~3 Å from the graphene surface (alkyl chains parallel to the zigzag main axis) with adjacent diazirine derivatives in antiparallel configuration, assuming an interdigitation pattern for the alkyl chains with inter-distance of 4.3 Å. Then geometric optimization of the supramolecular 2D architecture of the MBB-1 or MBB-2 was performed (see Supplementary Fig. 9).

DFT calculations and estimation of the doping. We performed DFT calculations under periodic boundary conditions using the SIESTA software package[11] to evaluate the charge density redistribution as well as the influence of the electrostatic potential induced by the SL on the WF of graphene. The Perdew-Burke-Ernzerhof functional (GGA) has been chosen for the description of the exchange-correlation as it was shown to correctly describe interfacial electronic structure and charge transfer between graphene and various donor/acceptor physisorbed on graphene (and other) surfaces.[12,13] A DZP basis set is used to describe the valence electrons and Troullier-Martins pseudopotentials are used to describe the core electrons. The mesh cutoff was set to 250 Ry and we used a k-sampling of 9×9×1 in the Monkhorst-Pack scheme. This setup gave a WF of 4.6 eV for the pristine graphene layer, which is in good agreement with experimental data.[7]

The work function of a substrate WF is defined as the energy required to extract an electron from the bulk to the vacuum level:

$$\mathrm{WF} = V_\infty - E_\mathrm{F} \tag{1}$$

where V_∞ is the electrostatic potential in vacuum and E_F is the Fermi level of graphene. The contribution of the interface potential to the work function shift can be estimated via the charge density difference $\Delta\rho$ at the interface:

$$\Delta\rho(z) = \rho_\mathrm{sys} - (\rho_\mathrm{SL} + \rho_\mathrm{graphene}) \tag{2}$$

where ρ_sys, ρ_SL, and ρ_graphene are the charge density of the whole system (interface), the SL and the graphene layer, respectively. The electrostatic potential ΔV_E associated to the charge density difference at the interface $\Delta\rho$ is obtained by a numerical integration of the Poisson equation:

$$\frac{\mathrm{d}^2 V_\mathrm{E}}{\mathrm{d}z^2} = -\frac{\Delta\rho}{\varepsilon_0} \tag{3}$$

The work function shift ΔWF can be expressed as a combination of two main contributions:

$$\Delta\mathrm{WF} = \Delta V_\mathrm{SL} + \phi = \Delta V_\mathrm{SL} + \Delta V_\mathrm{E} + \Delta V_\mathrm{graphene} \tag{4}$$

where ΔV_SL is a shift of the electrostatic potential induced by the intrinsic dipole moment of the SL, and ϕ is the potential change upon adsorption of the SL on graphene. The latter can be decomposed in two terms, namely the geometric rearrangement of the substrate $\Delta V_\mathrm{graphene}$ and the electronic reorganization or charge transfer at the interface ΔV_E.[14]

Upon physisorption of the SL on graphene, no geometric restructuration of the carbon atoms occurs ($\Delta V_\mathrm{graphene} = 0$). Therefore, the change in work function, ΔWF, can be expressed in terms of the local electrostatic potential associated to the charge density redistribution ΔV_E at the interface, and the intrinsic dipole moment of the SL, ΔV_SL. By calculating the potential profile across the molecules while keeping the geometry fixed, the SL contribution can be computed. The charge density redistribution can then be calculated by subtracting ΔV_{SL} from ΔWF. Besides, the intrinsic dipole moment of the SL can be calculated knowing the electric dipole of the molecules in the SL. Indeed, in the Helmholtz model, the molecular contribution is directly proportional to the electric dipole of the molecules along the axis normal to the graphene surface, μ:

$$\Delta V_{\mathrm{SL}} = \frac{-\mu e}{\varepsilon_0 S} \tag{5}$$

where e is the elementary charge, ε_0 the vacuum permittivity, and S the surface area of the unit cell.

Microelectrostatic Calculations. To gain further insight on the WF shift due to the molecular adsorbate we performed classical microelectrostatic (ME) calculations.[15] An accurate polarizable model based on atomic ESP charges and polarizabilities has been built from DFT calculations. The molecular polarizability tensor has principal components α_1=71, α_2=45 and α_3=37 Å^3 at the B3LYP/6-311G** level, where the first principal axis is approximately oriented along the alkyl chain, and the third one points normal to the adlayer plane. Induced dipoles at all atoms of the molecular adlayer have been determined self consistently, i.e. fully accounting for their mutual interactions. Periodic boundary conditions are taken into account by computing the interact

tions between the 2D graphene-adlayer cell and its periodic replica within a 50 nm cut-off radius, ensuring converged electrostatic sums.[16]

Supplementary Note 1

Synthetic procedures and characterizations.

3-(3-(octadecyloxy)phenyl)-3-(trifluoromethyl)-3*H*-diazirine (MBB-1). To a solution of 3-(3-(trifluoromethyl)-3H-diazirin-3-yl)phenol (S1, 1.0 eq) in 60 mL of acetone was added 1-bromooctadecane (1.5 eq) and K_2CO_3 (3.0 eq). After refluxed with vigorously stirring overnight, the reaction mixture was filtrated and washed thoroughly with dichloromethane. The combined organic solutions were then evaporated to give the oil-like crude product, which was purified by column chromatography over silica gel by first using hexane as eluent to wash away the excessive 1-bromooctadecane, and then using hexane/DCM (10 : 1) to give the title compound as a white solid (3.20 g, yield: 65%). FD-MS (8 kV) *m*/*z*: Calcd for $C_{26}H_{41}F_3N_2O$: 454.3; Found: 454.2 (100%) $[M]^+$. ^1H NMR (300 MHz, CD_2Cl_2, ppm) δ 7.31 (t, J = 8.1 Hz, 1H), 6.95 (ddd, J = 8.4, 2.5, 0.9 Hz, 1H), 6.77 (d, J = 7.7 Hz, 1H), 6.68 (s, 1H), 3.94 (t, J = 6.5 Hz, 2H), 1.83 – 1.68 (m, 2H), 1.52 – 1.14 (m, 30H), 0.88 (t, J = 6.9 Hz, 3H). ^{13}C NMR (75 MHz, CD_2Cl_2, ppm) δ 160.07, 130.85, 130.61, 124.59, 120.96, 118.95, 116.27, 113.35, 68.83, 32.54, 30.30, 30.26, 30.20, 30.17, 29.97, 29.96, 29.72, 26.54, 23.30, 14.48.

3-(octadecyloxy)benzaldehyde (S9). To a solution of 3-hydroxybenzaldehyde (2.5 g, 1.0 eq, 20 mmol) in 60 mL of acetone was added 1-bromooctadecane (10.0 g, 1.5 eq, 30 mmol) and K_2CO_3 (8.3 g, 3.0 eq, 60 mmol). The mixture was heated to 60 °C with vigorous stirring overnight. After cooling to room temperature, the reaction mixture was filtrated and washed thoroughly with DCM. The combined organic solution was then evaporated to give an oil-like crude product, which was purified by column chromatography over silica gel by first using hexane as eluent to wash away the excessive 1-bromooctadecane, and then using hexane/DCM (4 : 1) to give the title compound as a white solid (6.70 g, yield: 89%). FD-MS (8 kV) *m*/*z*: Calcd for $C_{25}H_{42}O_2$: 374.3; Found: 374.1 (100%) $[M]^+$. HRMS (ESI) *m*/*z*: Calcd for $C_{25}H_{42}O_2Na$: 397.3083; Found: 397.3073 $[M + Na]^+$. ^1H NMR (300 MHz, CD_2Cl_2, ppm) δ 9.95 (s, 1H), 7.47 – 7.41 (m, 2H), 7.39 – 7.34 (m, 1H), 7.21 – 7.14 (m, 1H), 4.02 (t, J = 6.6 Hz, 2H), 1.91 – 1.69 (m, 2H), 1.52 – 1.14 (m, 30H), 0.88 (t, J = 6.9 Hz, 3H). ^{13}C NMR (75 MHz, CD_2Cl_2, ppm) δ 192.59, 138.47, 130.55, 123.39, 122.13, 113.51, 68.95, 32.49, 30.26, 30.22, 30.16, 30.14, 29.93, 29.70, 26.53, 23.26, 14.45.

2,2,2-trifluoro-1-(3-(octadecyloxy)phenyl)ethanol (P-1). The synthesis procedure was following the literature[19]. 3-(Octadecyloxy)benzaldehyde S2 (370 mg, 1.0 eq, 1 mmol) and $TMSCF_3$ (0.200 mL, 1.35 eq, 1.35 mmol) were dissolved in anhydrous DMF (10 mL) in a 50-mL round-bottom flask. To this solution was added K_2CO_3 (20 mg, 15% mol, 0.15 mmol), and the mixture was stirred vigorously at room temperature overnight. The reaction mixture was quenched with 20 mL aqueous solution of HCl (1.0 M), stirred for 1 hour, and then extracted with diethyl ether (3 × 30 mL). The combined organic layers were finally washed with brine, dried over anhydrous Na_2SO_4, and then concentrated under reduced pressure. The crude product was purified by column chromatography over silica gel with hexane/DCM (3 : 1) as eluent to give the title compound (380 mg, yield: 85%) as a white solid. FD-MS (8 kV) *m/z*: Calcd for $C_{26}H_{43}O_2F_3$ 444.3; Found 444.3 (100%) $[M]^+$. HRMS (ESI) *m/z*: Calcd for $C_{26}H_{43}O_2F_3Na$: 467.3113; Found: 467.3100 $[M + Na]^+$. ^1H NMR (300 MHz, CD_2Cl_2, ppm) δ 7.32 (t, J = 8.2 Hz, 1H), 7.08 – 6.99 (m, 2H), 6.97 – 6.91 (m, 1H), 5.01 (q, J = 6.8 Hz, 1H), 3.97 (t, J = 6.6 Hz, 2H), 2.40 (br, 1H), 1.90 – 1.67 (m, 2H), 1.58 – 1.15 (m, 30H), 0.89 (t, J = 6.6 Hz, 3H). ^{13}C NMR (75 MHz, CD_2Cl_2, ppm) δ 159.96, 136.15, 130.16, 126.83, 123.10, 119.97, 116.03, 114.14, 73.75, 73.32, 72.90, 72.48, 68.75, 32.53, 30.30, 30.27, 30.21, 30.19, 30.00, 29.97, 29.81, 26.59, 23.29, 14.48.

1-(1-chloro-2,2,2-trifluoroethyl)-3-(octadecyloxy)benzene (P-2). To a mixture of P-1 (147 mg, 0.33 mmol) and pyridine (32 mg, 0.40 mmol) was slowly added thionyl chloride (48 mg, 0.40 mmol) and catalytic amount of DMF (5 drops). The mixture was heated at 80 °C for 5 h. After cooling down to room temperature, the mixture was quenched by water and extracted with dichloromethane for three times The combined organic layers were washed with diluted HCl, water, and brine, and then dried over $MgSO_4$. The solvents were removed under reduced pressure and the residue was purified by column chromatography over silica gel (eluent: hexane/DCM = 20 : 1) to give the title compound (96 mg, yield: 63%) as a white solid. FD-MS (8 kV) *m*/*z*: Calcd for $C_{26}H_{42}ClF_3O$ 462.3; Found: 462.3 (100%) $[M]^+$. ^1H NMR (300 MHz, CD_2Cl_2, ppm) δ 7.32 (t, J = 7.9 Hz, 1H), 7.09 – 7.00 (m, 2H), 6.96 (ddd, J = 8.3, 2.5, 1.0 Hz, 1H), 5.14 (q, J = 6.9 Hz, 1H), 3.97 (t, J = 6.5 Hz, 2H), 1.89 – 1.68 (m, 2H), 1.52 – 1.15 (m, 30H), 0.88 (t, J = 6.9 Hz, 3H). ^{13}C NMR (175 MHz, CD_2Cl_2, ppm) δ 160.02, 133.90, 130.37, 126.47, 124.88, 123.30, 121.71, 121.23, 116.66, 115.48, 68.84, 59.46, 59.27, 59.07, 58.88, 32.53, 30.29, 30.26, 30.20, 30.17, 29.97, 29.77, 26.57, 23.29, 14.47.

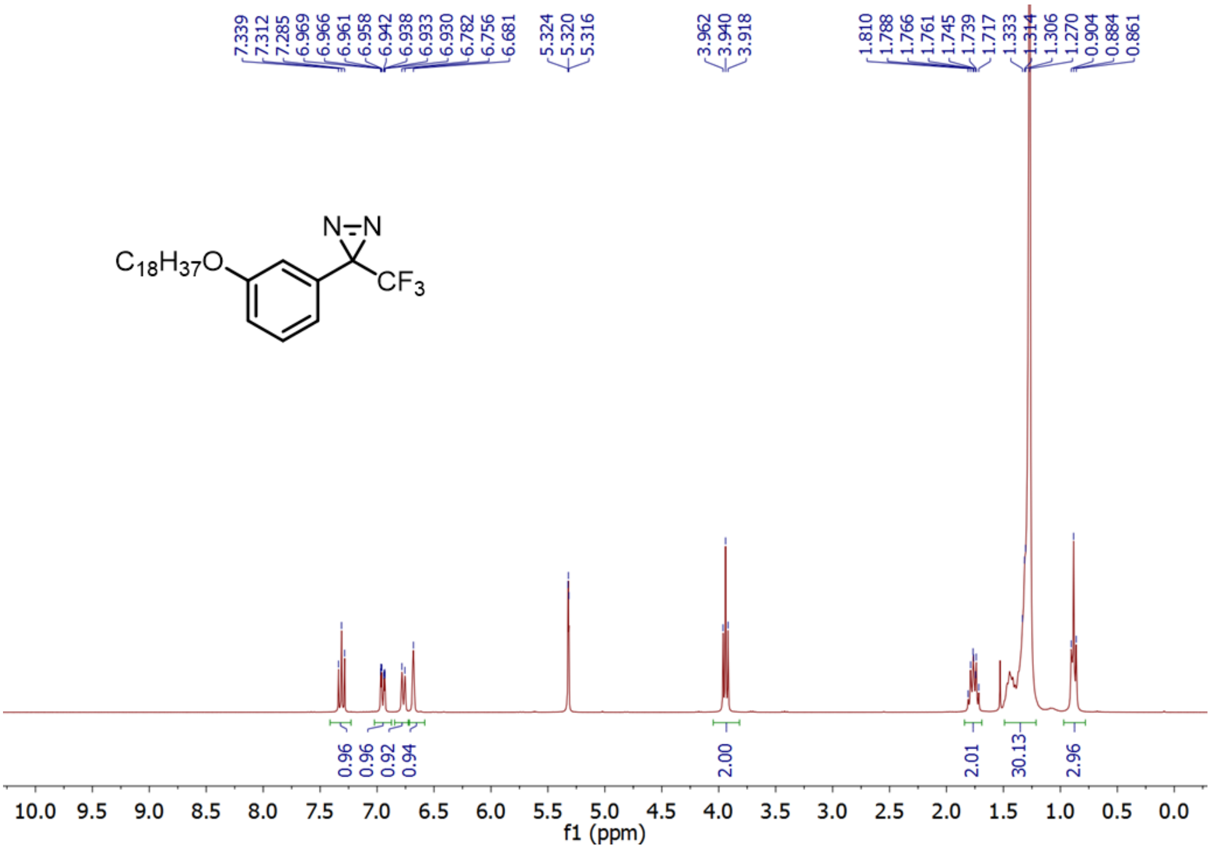

Supplementary Figure 14. ^{1}H nuclear magnetic resonance characterization of MBB-1. ^{1}H nuclear magnetic resonance spectroscopy analysis of MBB-1 (300 MHz, CD_2Cl_2). Inset: chemical structure of MBB-1.

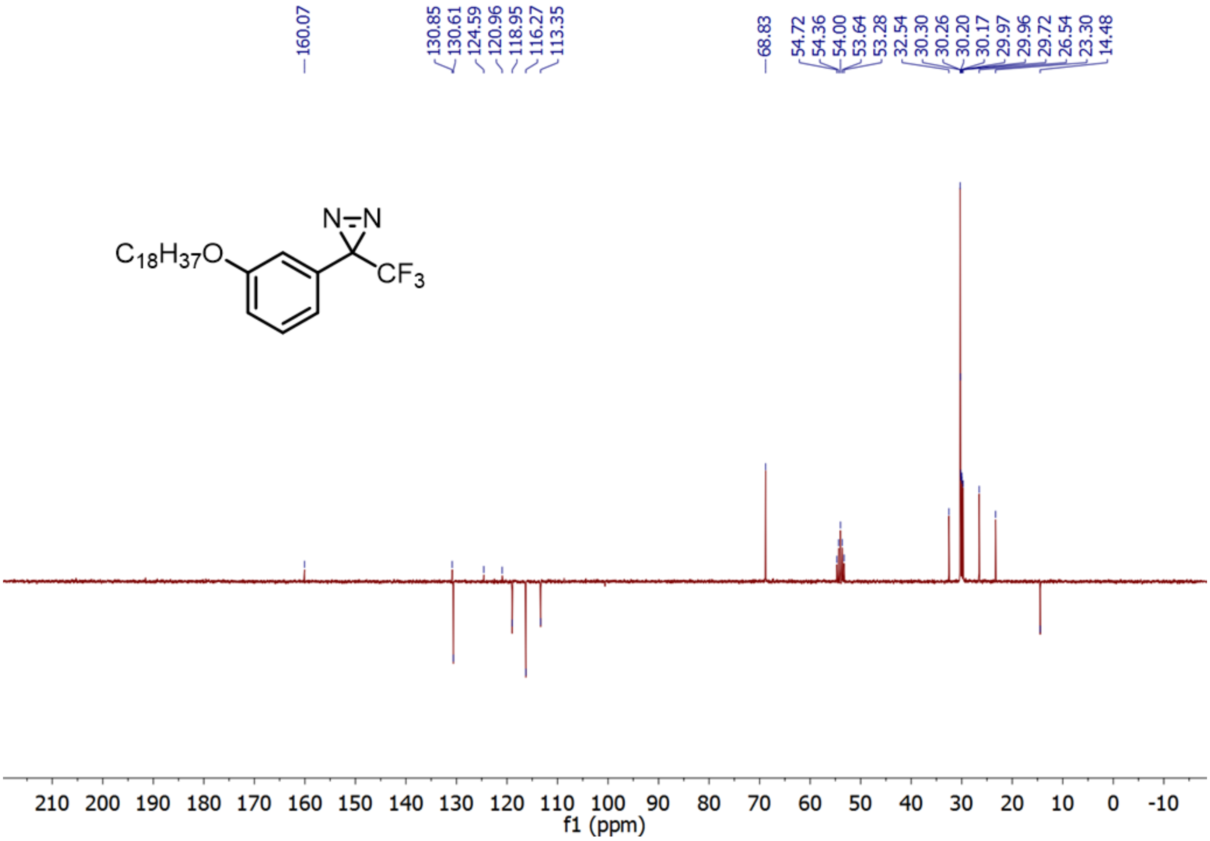

Supplementary Figure 15. ^{13}C nuclear magnetic resonance characterization of MBB-1. ^{13}C nuclear magnetic resonance spectroscopy analysis of MBB-1 (75 MHz, CD_2Cl_2). Inset: chemical structure of MBB-1.

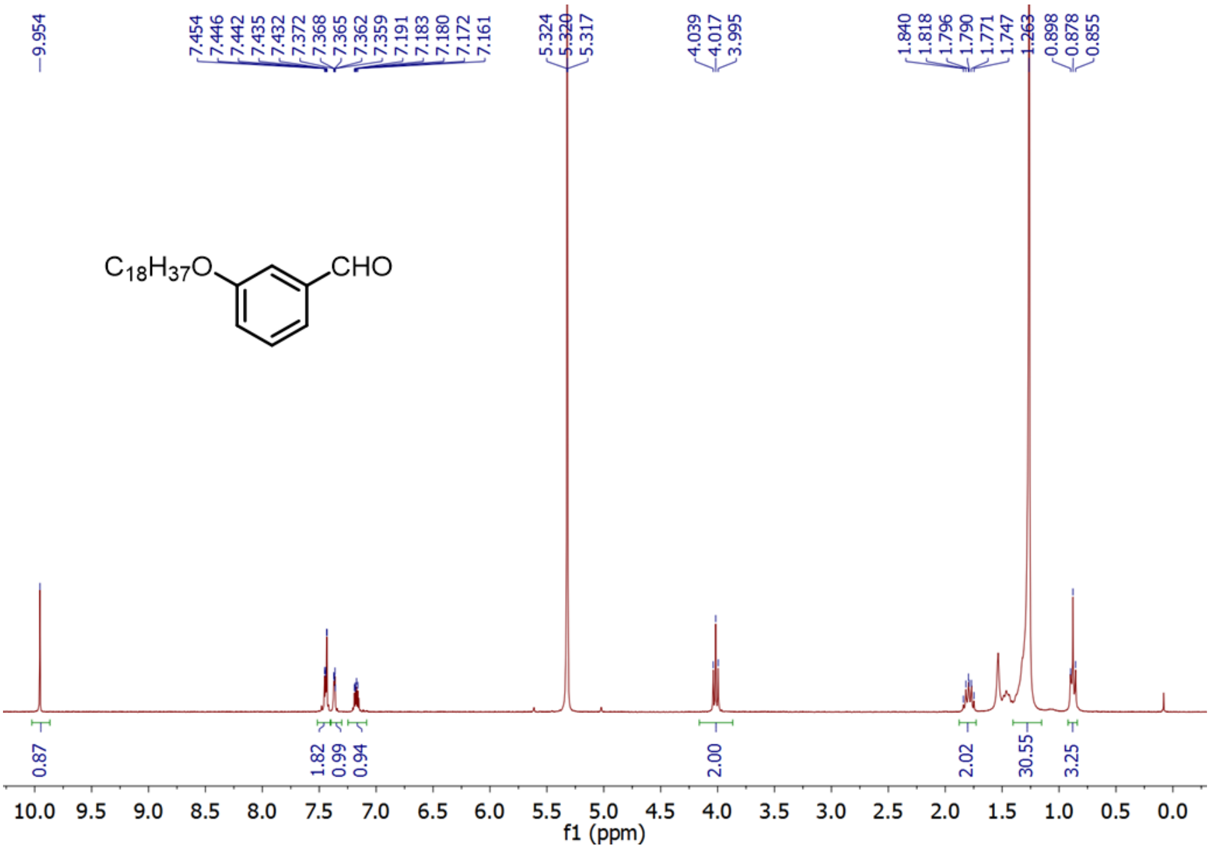

Supplementary Figure 16. ^{1}H nuclear magnetic resonance characterization of S9. ^{1}H nuclear magnetic resonance spectroscopy analysis of S9 (300 MHz, CD_2Cl_2). Inset: chemical structure of S9.

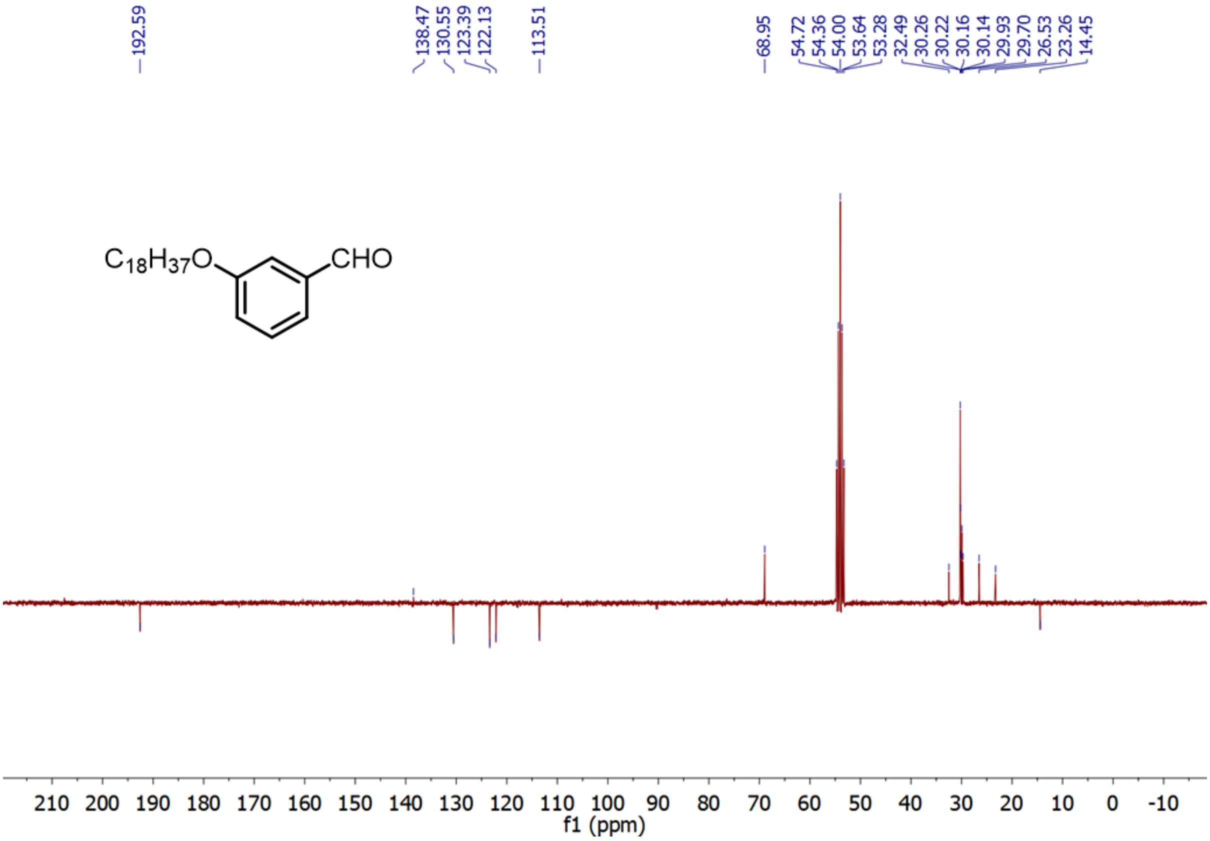

Supplementary Figure 17. ^{13}C nuclear magnetic resonance characterization of S9. ^{13}C nuclear magnetic resonance spectroscopy analysis of S9 (75 MHz, CD_2Cl_2). Inset: chemical structure of S9.

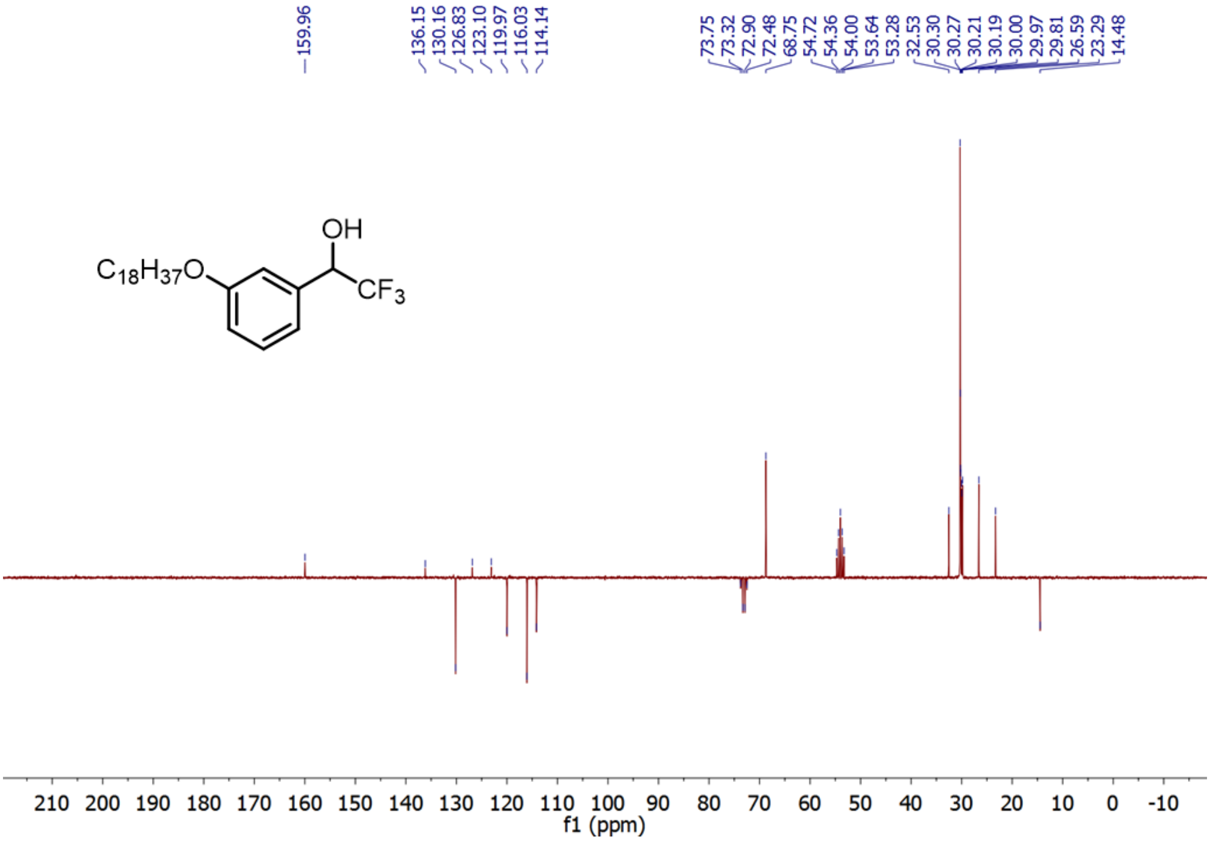

Supplementary Figure 18. ^{13}C nuclear magnetic resonance characterization of P-1. ^{13}C nuclear magnetic resonance spectroscopy analysis of P-1 (75 MHz, CD_2Cl_2). Inset: chemical structure of P-1.

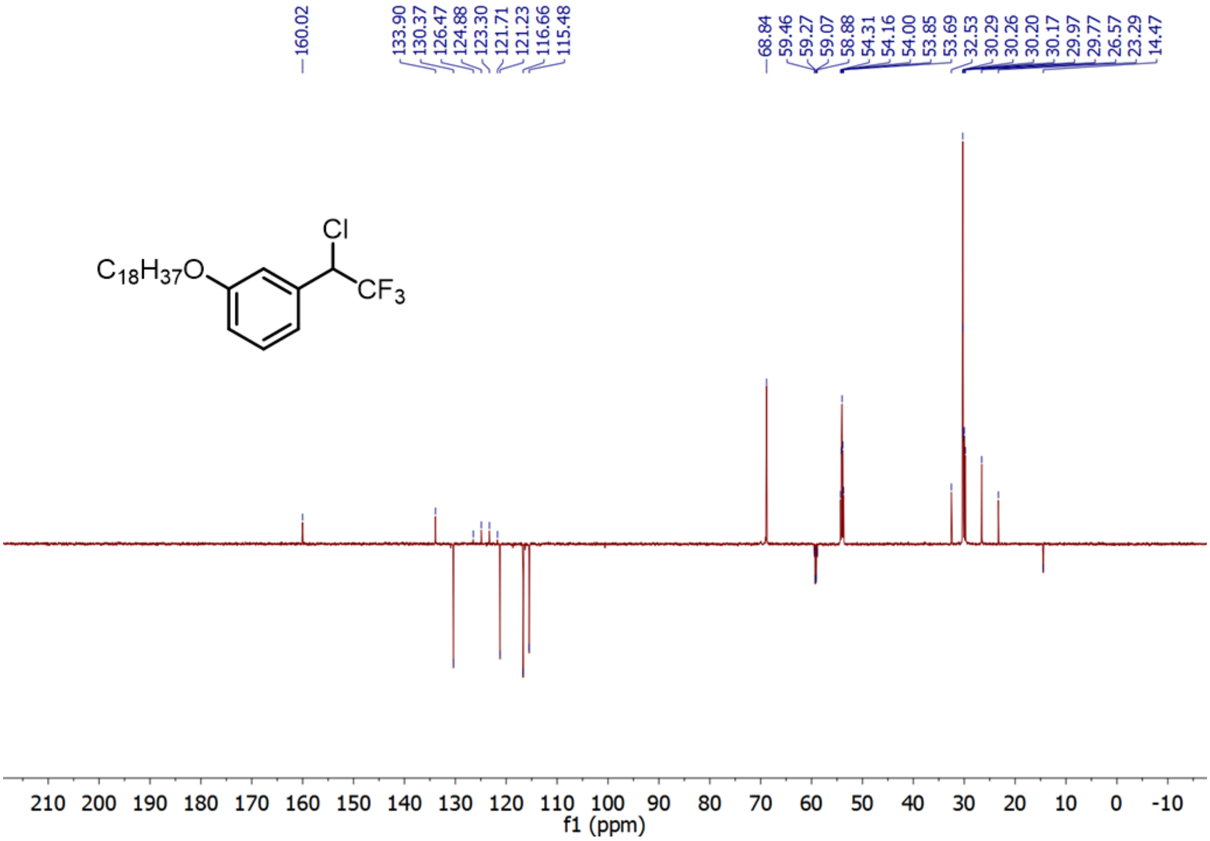

Supplementary Figure 19. ^{13}C nuclear magnetic resonance characterization of P-2. ^{13}C nuclear magnetic resonance spectroscopy analysis of P-2 (175 MHz, CD_2Cl_2). Inset: chemical structure of P-2.

Supplementary references

---

1. Balderschi, A., Baroni, S. & Resta, R. Band offsets in lattice-matched heterojunctions: A model and first-principles calculations for GaAs/AlAs. *Phys. Rev. Lett.* **61,** 734–737 (1988).
2. Coletti, C. *et al.* Charge neutrality and band-gap tuning of epitaxial graphene on SiC by molecular doping. *Phys. Rev. B* **81,** 235401 (2010).
3. Yan, J., Zhang, Y., Kim, P. & Pinczuk, A. Electric field effect tuning of electron-phonon coupling in graphene. *Phys. Rev. Lett.* **98,** 166802 (2007).
4. Froehlicher, G. & Berciaud, S. Raman spectroscopy of electrochemically gated graphene transistors: Geometrical capacitance, electron-phonon, electron-electron, and electron-defect scattering. *Phys. Rev. B - Condens. Matter Mater. Phys.* **91,** 205413 (2015).
5. Samuels, A. J. & Carey, J. D. Molecular doping and band-gap opening of bilayer graphene. *ACS Nano* **7,** 2790–2799 (2013).
6. Wehling, T. O. *et al.* Molecular doping of graphene. *Nano Lett.* **8,** 173–177 (2008).
7. Yu, Y.-J. *et al.* Tuning the graphene work function by electric field effect. Supplementary Information. *Nano Lett.* **9,** 3430–3434 (2009).
8. Ha, T.-J. *et al.* Transformation of the Electrical Characteristics of Graphene Field- Effect Transistors with Fluoropolymer. *ACS Appl. Mater. Interfaces* **5,** 16–20 (2013).
9. Besler B. H., Merz K. M., J. & A., K. P. Atomic charges derived from semiempirical methods. *J. Comput. Chem.* **11,** 431–439 (1990).
10. Frisch, M. J. *et al.* Gaussian 09, Revision D.01. Gaussian, Inc., Wallingford, CT, 2009.
11. Soler, J. M. *et al.* The SIESTA method for ab initio order-N materials simulation. *J. Phys. Condens. Matter* **14,** 2745-2779 (2002).
12. Cornil, D., Van Regemorter, T., Beljonne, D. & Cornil, J. Work function shifts of a zinc oxide surface upon deposition of self-assembled monolayers: a theoretical insight. *Phys. Chem. Chem. Phys.* **16,** 20887–20899 (2014).
13. Christodoulou, C. *et al.* Tuning the work function of graphene-on-quartz with a high weight molecular acceptor. *J. Phys. Chem. C* **118,** 4784–4790 (2014).
14. Heimel, G., Romaner, L., Br??das, J. L. & Zojer, E. Organic/metal interfaces in self-assembled monolayers of conjugated thiols: A first-principles benchmark study. *Surf. Sci.* **600,** 4548–4562 (2006).
15. D'Avino, G., Muccioli, L., Zannoni, C., Beljonne, D. & Soos, Z. G. Electronic polarization in organic crystals: A comparative study of induced dipoles and intramolecular charge redistribution schemes. *J. Chem. Theory Comput.* **10,** 4959–4971 (2014).
16. D'Avino, G., Vanzo, D. & Soos, Z. G. Dielectric properties of crystalline organic molecular films in the limit of zero overlap. *J. Chem. Phys.* **144,** 34702 (2016).

17. Kim, K. & Jordan, K. D. Comparison of Density Functional and MP2 Calculations on the Water Monomer and Dimer. *J. Phys. Chem.* **98,** 10089–10094 (1994).
18. Lawrence, E. J. *et al.* 3-Aryl-3-(trifluoromethyl)diazirines as Versatile Photoactivated 'Linker' Molecules for the Improved Covalent Modification of Graphitic and Carbon Nanotube Surfaces. *Chem. Mater.* **23,** 3740–3751 (2011).
19. Prakash, G. K. S. *et al.* Facile synthesis of TMS-protected trifluoromethylated alcohols using trifluoromethyltrimethylsilane (TMSCF3) and various nucleophilic catalysts in DMF. *J. Org. Chem.* **71,** 6806–6813 (2006).